

F. Dupoirieux, N. Bertier, C. Guin,
L.-H. Dorey
(ONERA)
K.P. Geigle, C. Eberle, P. Gerlinger
(DLR)

E-mail: francis.dupoirieux@onera.fr

DOI : 10.12762/2016.AL11-07

Methodology for the Numerical Prediction of Pollutant Formation in Gas Turbine Combustors and Associated Validation Experiments

For aircraft engine manufacturers the formation of pollutants such as NO_x or soot particles is an important issue because the regulations on pollutant emissions are becoming increasingly stringent. In order to comply with these regulations, new concepts of gas turbine combustors must be developed with the help of simulation tools. In this paper we present two different strategies, proposed by ONERA and DLR respectively, to simulate soot or NO_x formation in combustors. The first one is based on simple chemistry models allowing significant effort to be spent on the LES description of the flow, while the second one is based on more accurate, but also more expensive, models for soot chemistry and physics. Combustion experiments dedicated to the validation of these strategies are described next: The first one, performed at DLR, was operated at a semi-technical scale and aimed at very accurate and comprehensive information on soot formation and oxidation under well-defined experimental conditions; the second one, characterized at ONERA, was aimed at reproducing the severe conditions encountered in realistic gas turbine combustors. In the third part of the paper the results of combustion simulations are compared to those of the validation experiments. It is shown that a fine description of the physics and chemistry involved in the pollutant formation is necessary but not sufficient to obtain quantitative predictions of pollutant formation. An accurate calculation of the turbulent reactive flow interacting with pollutant formation and influencing dilution, oxidation and transport is also required: when the temperature field is correctly reproduced, as is the case of the ONERA simulation of the DLR combustor, the prediction of soot formation is quite satisfactory while difficulty in reproducing the temperature field in the TLC combustor leads to overestimations of NO_x and soot concentrations.

Introduction

The combustion inside gas turbine burners generates emissions of the greenhouse gas CO₂, as well as pollutants such as NO_x, CO, soot particles and UHC (Unburned HydroCarbons). Increasingly stringent regulations are being introduced to require lower emissions in newly manufactured aircraft engines. A decrease in CO₂ emissions is achieved through various paths, among these the increase in the OPR (Operating Pressure Ratio) of the gas turbine. The increase in the pressure inside the GT (Gas Turbine) combustor leads to a better thermodynamic efficiency of the engine and also tends to minimize the effect of incomplete combustion and therefore to limit CO and UHC emissions.

On the other hand, this pressure increase leads to a higher combustor inlet temperature, which results in turn in a higher temperature inside the combustor and thus greatly favors NO_x formation. The incorporation of more stringent regulations for NO_x emissions is therefore a very challenging task, which requires the development of new combustor concepts. Figure 1, extracted from Ralph and Baker [1], shows the evolution of the regulations as well as the mid-term and long-term goals for NO_x emissions. In figure 1, past and present regulations have a positive slope of tolerated emissions with increasing OPR in order to not impede the development of engines with a high OPR. However, in future this slope will be smaller: this makes the compliance with future NO_x regulations much more difficult for high OPR engines.

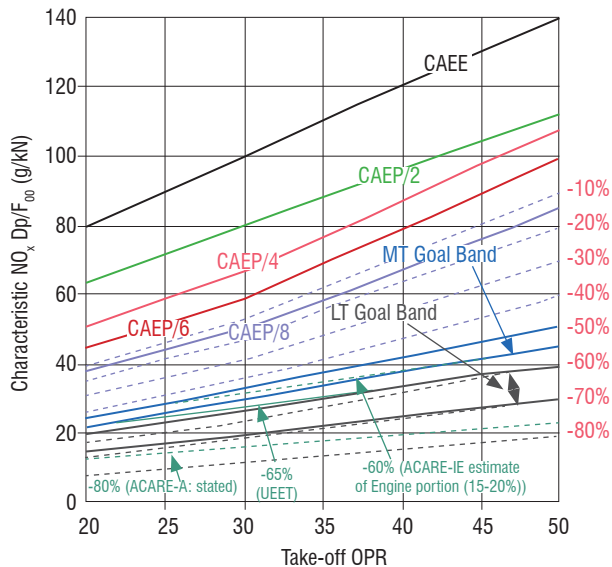


Figure 1 – Regulations and mid-term/long-term (MT/LT) goals concerning the NOx emissions per unit engine thrust as a function of the OPR at take off

Until now, the regulation for aircraft emissions of particulate matter, including soot, was based on the evaluation of the Smoke Number (SN) [2], which is quite rough considering that parameters such as particle size, particle number density or surface reactivity of particles are not accessible by the SN, but are essential to define the harmfulness of these emitted particles. In recent engine developments, the size of emitted particles decreased and the particle number simultaneously increased, while the filters used for measuring SN are significantly less sensitive to small particles. For that reason, significant efforts are spent to define measurement procedures for engine certification, which will be routinely used at the industrial level and replace the SN evaluation to yield more detailed information on the emitted particulate matter (Delhay *et al.* [3], Black *et al.* [4] and Petzold *et al.* [5]). This expected change in the regulations for particulate matter emissions is another point that must be tackled by engine manufacturers, without compromising achievements in NOx emission minimization.

In order to design new engines complying with these future regulations, aircraft manufacturers need support from numerical tools that are able to predict pollutant formation, especially NOx at high pressure and soot particles, which largely contribute to the harmful particles emitted by the combustion chamber. The design and development of low NOx combustors based on lean premixed combustion is particularly troublesome because they are prone to instabilities (see for example Cohen *et al.* [6], Lieuwen [7]). RQL (Rich Quick quench Lean) combustors (Feitelberg *et al.* [8], Jermakian *et al.* [9]) are less sensitive to thermoacoustics because the fuel rich section ensures combustion stability but, unfortunately, the potential for NOx reduction is limited. The more recently developed TAPS devices (Stickles and Barrett [10]) include pilot injection to stabilize the combustion and a main multi-hole injector to prompt the fuel-air mixing. The determination of the best geometry and optimal distribution between pilot and main injection at different flight regimes is very challenging.

Many attempts to predict NOx formation in gas turbine combustors can be found in the literature. Some are based on steady-state methods (Riesmeier *et al.* [11], for example) and contain an accurate description of the chemistry, but are not designed to capture combustion instabilities. Others are based on LES (Large Eddy Simulation) and can provide insight into instability mechanisms, but

contain relatively simple chemistry (Schmitt *et al.* [12], for example). One possible approach to combine LES with a complex chemistry, including NOx formation, is tabulated chemistry (Godel *et al.* [13], for example). The validation of the methodology for these NOx simulations is not an easy task, because generally NO or NOx measurements are only achieved by gas sampling at the exit of the combustors (Ibas *et al.* [14], Landman *et al.* [15], for example). Sometimes, the sampling probe is moved inside the flame to obtain information at different locations, but in most examples the flame configuration is far from that encountered in gas turbine combustors (Li and Williams [16], Sze *et al.* [17], for example), moreover, the flow field governing the global flame behavior is significantly affected by such intrusive measurement techniques. Spatially resolved, non-intrusive NO measurements by LIF (Laser Induced Fluorescence) have also been carried out in flames (Meier *et al.* [18], Sick *et al.* [19], Meier *et al.* [20], Bessler *et al.* [21], van Essen *et al.* [22], for example), but again the configuration (pure diffusion or pure premixed flames) and the experimental conditions (laminar or low pressure flames, fuel reduced to pure CH₄ or H₂) are far from those of gas turbine combustors.

Some difficulties also appear in the development of numerical tools for soot predictions. The physics of soot formation is known to be very complex because it involves complex chemical mechanisms occurring both in the gaseous phase and at the interface between the small solid soot particles and the surrounding gaseous phase, see for example Bockhorn [23]. Developing reliable numerical tools for soot prediction requires the physical submodels to be adequately selected, in order to obtain the best compromise between accuracy and computation cost. Considering the high complexity of the phenomena that must be reproduced by the soot models, the numerical tool must be carefully validated by comparison with experiments. In the past, soot formation was first studied experimentally in laminar flames, in order to facilitate the measurements and to discard the additional complexity of turbulence; see for example Santoro *et al.* [24], Vandsburger *et al.* [25], Quay *et al.* [26], McEnally and Pfefferle [27]. Experimental studies in laminar flames are still being achieved, mainly to scrutinize the influence of pressure and/or mixture ratio on soot formation (Arana *et al.* [28], McCrain and Roberts [29], Thomson *et al.* [30], Desgroux *et al.* [31], Joo and Gülder [32]). These experiments serve to validate, without difficulties induced by the fluid flow complexity, physical models for soot formation intended to be introduced in CFD codes (Leung *et al.* [33], Blacha *et al.* [34]). Soot formation has also been experimentally studied in unsteady and turbulent flames, which provide conditions more resembling technical burners (Shaddix and Smyth [35], Qamar *et al.* [36], Lemaire *et al.* [37], Henriksen *et al.* [38], Köhler *et al.* [39], Mueller *et al.* [40], Geigle *et al.* [41-43]). In parallel, some attempts to simulate the soot formation in unsteady or turbulent flames have been made (Said *et al.* [44], Pitsch *et al.* [45], Zamuner and Dupoirieux [46], Yoo and Im [47], Lignell *et al.* [48], Narayanan and Trouvé [49], Köhler *et al.* [39], Bisetti *et al.* [50], Mueller and Pitsch [51], Attili *et al.* [52]). Nowadays, unsteady simulations of the DNS or LES type yield satisfactory results concerning the description of the turbulent flow, but are not yet able to reliably predict soot distributions, mainly because it is very difficult to correctly predict the concentration of soot precursors, which are made up of minor species such as acetylene (C₂H₂), benzene (C₆H₆), and polycyclic aromatic hydrocarbons (PAH). The prediction of the size distribution of the soot particles is particularly challenging. It can be obtained by resolution of transport equations, one for each size section, as obtained by Köhler *et al.* [39], or for moments of the soot particle size distribution as done by Mueller and Pitsch [51], or by a Lagrangian approach as was done by Zamuner and Dupoirieux [46], or Dupoirieux *et al.* [53]. Whatever

	DLR experiment	ONERA-SNECMA experiment
Main flow features	<ul style="list-style-type: none"> • C₂H₄/air non-premixed swirled injection • Optional air dilution in the downstream part of the combustor • Pressure from 1 to 5 bar 	<ul style="list-style-type: none"> • Two-swirl air injection including pilot and multi-holes injectors for liquid kerosene • Pressure from 4 to 20 bar
Optical or sampling measurements and visualizations	<ul style="list-style-type: none"> • PIV velocity measurements (non-reactive and hot conditions) • CARS temperature measurements with complete local statistics • OH and PAH PLIF visualizations • LII soot measurements 	<ul style="list-style-type: none"> • CARS temperature measurements with complete local statistics • OH and PAH PLIF visualizations • LII soot measurements • NO and NO_x emission index by gas sampling and analysis

Table 1 – Main features of the validation experiments

the method, the computational effort is significant with a large number of transport equations to solve in the first case and a large number of fluid particles to track in the second case. According to the available computational power, different strategies can be used to apply numerical soot prediction to the practical situation of GT combustors: soot simulation in post-processing as used by Barths *et al.* [54], flamelet approach as used by Riesmeier *et al.* [11], or LES as used by Mueller and Pitsch [55]. In this paper we propose two strategies for soot prediction in GT combustors, which can be considered as a good compromise between accuracy and computational effort.

The next section presents two possible numerical methodologies, proposed by ONERA and DLR respectively, for the simulation of soot and NO_x formation. Section "Experiments for the validation of the numerical strategies of pollutant prediction" describes experiments for the validation of these methodologies: the first one, performed at DLR (Geigle *et al.* [42]), can be considered as a semi-technical scale experiment and focuses on soot; the second one, carried out at ONERA, reproduces the real conditions encountered in a GT combustor. Section "Calculation of the DLR burner for validation purposes" displays validations resulting from the comparison of the simulations with the experiment of Geigle *et al.* [42,43], and Section "ONERA Calculation of the TLC combustor" presents the numerical results corresponding to the ONERA experiment. To clarify the presentation tables 1 and 2 hereafter summarize the validation experiments and calculations described in this paper.

Physical models and associated numerical methodology

ONERA methodology

The numerical methodology proposed for the prediction of soot formation in GT combustors is based on LES simulations carried out by the CEDRE software (Refloch *et al.* [56]). The resolution of the compressible Navier-Stokes equations for the gaseous phase is achieved by the solver CHARME and the evaporating fuel droplets are tracked using the Lagrangian solver SPARTE. These two solvers of CEDRE operate in a two way coupling mode: On the one hand, CHARME provides SPARTE with all of the information necessary to calculate the instantaneous drag force acting on droplets and the heat flux leading to heating and vaporization of the liquid phase; on the other hand, SPARTE provides CHARME with the mass flux, momentum, energy and turbulent kinetic energy delivered to the gaseous phase from the liquid droplets. The SPARTE module is used only in the second calculation presented in this paper, since the first burner studied (DLR combustor) is operated with gaseous fuel, i. e., ethylene.

In our LES calculations the usual Smagorinsky viscosity is used to take into account the effect of turbulent structures smaller than the mesh size and a law of the wall adapted to the turbulence subgrid model yields the stress tensor on the walls. The interaction between chemistry and turbulence is tackled with the help of the Artificially Thickened Flame model (ATF) for LES (Selle *et al.* [57]). In this approach the thickening factor F and the efficiency function E are introduced into the transport equations of the reactive species, to modify the diffusion and chemical term. The transport equation of the k^{th} species is then written as:

Simulation \ Experiment	DLR experiment	ONERA-SNECMA experiment
DLR	<ul style="list-style-type: none"> • 3D URANS • Detailed finite rate chemistry for soot precursors • Sectional PAH model • Two-equation soot model 	Comparison with: <ul style="list-style-type: none"> • OH visualizations • LII soot visualizations
ONERA	<ul style="list-style-type: none"> • 3D LES • Thickened flame model and tabulated chemistry • Soot model of Leung 	Comparison with: <ul style="list-style-type: none"> • 3D LES • Thickened flame model and tabulated chemistry with β PDF • Soot model of Leung • Definition of a specific progress variable for thermal NO prediction Comparison with: <ul style="list-style-type: none"> • CARS temperature measurements • LII soot measurements • NO and NO_x emission index

Table 2 – Validation calculations

$$\frac{\partial \bar{\rho} \tilde{Y}_k}{\partial t} + \frac{\partial (\bar{\rho} \tilde{u}_i \tilde{Y}_k)}{\partial x_i} = \frac{\partial}{\partial x_i} \left\{ \bar{\rho} \left[FED_k + (1 - \alpha) D_k' \right] \frac{\partial \tilde{Y}_k}{\partial x_i} \right\} + \frac{E}{F} \dot{\omega}_k$$

$$\text{with } F = 1 + \alpha (F^{\max} - 1) \quad (1)$$

In this equation, α is a sensor function varying from 0 far from the flame (low values of $|\dot{\omega}_k|$) to 1 inside the flame (high values of $|\dot{\omega}_k|$). F^{\max} is the parameter that determines the artificial thickening of the simulated flame and E is a function that takes values equal to 1 far from the flame and greater than 1 inside the flame. This function is aimed at recovering the effect of the flame folding lost by the artificial thickening and in our calculations its formulation is that described by Colin *et al.* [58]. In the numerical model, the diffusion coefficient inside the flame is equal to FED_k , where D_k is the physical laminar diffusion coefficient and FE is a factor much greater than 1, and far from the flame it is equal to D_k' , the small scale turbulent diffusion coefficient given by the Smagorinsky formulation. As indicated in [57], a value of 25 for F^{\max} seems reasonable to correctly resolve the flame front in the usual LES computation grids.

The source term $\dot{\omega}_k$ is usually governed by the chemical kinetics, which can be simplified if only the main steps of the fuel oxidation are taken into account. However, when soot formation has to be calculated, the situation is more complicated because the concentration of minor species, such as C_2H_2 or C_6H_6 , which are soot precursors, or OH, which is a soot oxidizer, must be known. That means that a detailed chemistry including a large number of chemical species must be considered in the calculation. In order to avoid the resolution of a large number of transport equations for the chemical species, a tabulated chemistry approach is used in conjunction with the ATF model. Tabulated chemistry has been extensively used to simulate turbulent combustion in the last decades, see for example Maas and Pope [59], Gicquel *et al.* [60], Van Oijen *et al.* [61], Fiorina *et al.* [62] and Kuenne *et al.* [63]. From the theoretical point of view, the tabulated chemistry is well adapted to the opposite cases of combustion, i. e., premixed flames and diffusion flames, for which two different types of flamelet manifolds can be created, but not to intermediate situations of partially premixed flames that can be encountered in GT combustors. However, it can be shown (Vreman *et al.* [64]) that determining the features of a partially premixed flame from a set of laminar premixed flamelets covering a large domain of mixture ratios leads in practice to satisfactory results. Therefore our approach of tabulated chemistry is based on a premixed flamelet manifold indexed by two parameters: the progress variable C and the mixture fraction Z . Before normalization, the progress variable is defined as

$$C = \frac{Y_{CO}}{M_{CO}} + \frac{Y_{CO_2}}{M_{CO_2}} + \frac{Y_{H_2O}}{M_{H_2O}} \quad (2)$$

For a given value of the mixture fraction Z the progress variable C monotonically evolves from 0 in the fresh gases to a maximum value $C^{\max}(Z)$. This maximum value is commonly referred to as $C|_{eq}$ considering that species included in the definition of C have reached chemical equilibrium. The normalized progress variable c with values within the interval [0,1] is finally defined as

$$c = \frac{C}{C|_{eq}} \quad (3)$$

Note that for the simulation of NOx formation the definition of C must be adapted to take into account the large characteristic time scales associated with the thermal NO mechanism. In that case, an additional term with the mass fraction of NO is introduced in Eq. (2), as indicated in section "Calculation of NOx emissions".

The mixture fraction Z is defined as

$$Z = Y_C + Y_H \quad (4)$$

Y_C (respectively Y_H) is the mass fraction of carbon (respectively hydrogen) atoms, whatever their molecular combination. Z is obviously varying between 0, in points where no fuel and no species resulting from the fuel combustion are present (oxidizer side), to 1, where only unburnt fuel or non-oxidized species resulting from the fuel cracking are present (fuel side).

Transport equations for the main species, i. e., fuel, O_2 , CO, CO_2 , H_2O and N_2 , are solved with a reaction source term calculated as

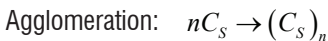
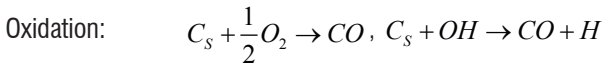
$$\dot{\omega}_k = \dot{\omega}_k^{TAB}(c, Z) + \frac{Y_k^{TAB}(c, Z) - \tilde{Y}_k}{\tau} \quad (5)$$

where the superscript TAB corresponds to values picked in the flamelet manifold and τ is a characteristic time linked to the chemistry (see Boucher *et al.* [65]). The last term of this equation is introduced to prevent departures of the concentrations calculated with the transport equations from the values given by the table for the same indexing parameters c and Z . In practice this correction term, introduced only for numerical reasons, is small in absolute value compared to the reaction source term picked from the table. The concentrations of all minor species such as NOx, soot precursors or soot oxidizers, i. e., NO, NO_2 , C_2H_2 , C_6H_6 , OH, are directly picked from the chemical table. The resolution of transport equations for the main species rather than picking their concentrations in the chemical table is necessary to account for diffusion properties not linked directly to those of c and Z . The progress variable C is obtained through Eq. 2 from the concentration of the main species. Considering that a non-negligible part of the C and H atoms can be contained in non-transported species, Z is obtained by resolution of a transport equation with accurate inlet conditions deduced from the fuel composition. This equation describes the mixing between fuel and oxidizer and implicitly contains the assumption that all species have the same diffusion coefficient.

For soot predictions, simple models inducing a low CPU time have been considered: the model of Magnussen *et al.* [66], and the model of Leung *et al.* [33]. These models require two additional transport equations. For the Magnussen model, these equations concern the soot mass fraction Y_s and the number of inception nuclei per volume unit. In the Leung model two transport equations are solved to calculate the soot mass fraction Y_s and the number N of soot particles per mixture mass unit. Acetylene (C_2H_2) is the precursor of soot in the Leung model while fuel is the precursor in the Magnussen model. Soot oxidation is achieved by O_2 in both models, but in addition oxidation by OH is considered in the Leung model. After various tests on 1D flames, the Leung model has been selected at the expense of the Magnussen model, which turned out to be too rough. The Leung model takes into account the steps of nucleation, surface growth, oxidation and agglomeration:

	Reaction rate (kmol·m ⁻³ ·s ⁻¹)	Preexponential factor A (SI unit)	Temperature exponent β	Activation temperature T_a (K)
Nucleation	$K_n(T)[C_2H_2]$	0.1×10^5	0	21100
Surface growth	$K_g(T)[C_2H_2]$	1.4×10^4	0	12100
O ₂ oxidation	$K_{Oxid.O_2}(T) \cdot S \cdot [O_2]$	0.1×10^5	0.5	19680
OH oxidation	$K_{Oxid.OH}(T) \cdot S \cdot [OH]$	106	-0.5	0

Table 3 – Soot reaction kinetics



The notation C_s refers to carbon atoms included in soot particles. As it is written, the nucleation step means that one mole of acetylene can lead to two moles of carbon included in nascent soot particles. The source terms of the balance equations induced by these different steps can be found in the work by Leung *et al.* [33] and Lecocq *et al.* [67]. Kinetic details of nucleation, surface growth and oxidation reactions are listed in table 3.

In this table, S , which appears in the oxidation rates, refers to the total surface of soot particles per volume unit and the quantities $K_i(T)$ ($i=n, g, Oxid.O_2, Oxid.OH$) depend on T according to

$$K_i(T) = AT^\beta e^{-\frac{T_a}{T}}$$

The agglomeration rate is given by

$$\vec{I} = \left\langle \left(1 + \frac{u_0^2}{c_{ii}^2} \right) p\vec{u} + \vec{u}_0 \left(\rho_0 u^2 + \frac{p^2}{\rho c^2} \right) \right\rangle \quad (6)$$

where C_A is equal to 9, M_C is the molar mass of the carbon atom ($12 \cdot 10^{-3}$ kg), ρ_{soot} is the soot density (1800 kg/m³), κ is the Boltzmann constant and ρ is the mixture density.

To sum up the numerical methodology, transport equations with chemical source terms deduced from the tabulated chemistry and adapted to LES are solved for the main species, and the soot parameters, i. e., the soot volume fraction and the number of particles per mixture mass unit, are obtained from transport equations with source terms given by the Leung model. In these source terms the concentration of minor species, such as C_2H_2 or OH, is directly taken from the chemical tables. A similar methodology is used by other teams, see Cuenot *et al.* [68].

DLR methodology

Soot and PAH sub-models are implemented in the DLR code THETA. THETA is an unstructured finite-volume solver, which has been optimized for low Mach number combustion problems. Combustion is modeled by finite-rate chemistry, where a separate transport equation is solved for each species. Chemical reactions involving soot and PAHs are formulated in Arrhenius form and solved by the finite-rate chemistry model, in the same way as the chemistry of gas phase species, thereby allowing full coupling of soot, PAHs and the thermo-chemical state of the gas phase. The soot and PAH sub-models conserve both mass and atoms.

Chemical and physical processes of soot evolution and the corresponding modeling strategies followed by DLR are summarized in figure 2. The kinetics of gas phase species, including combustion and pyrolysis of small hydrocarbons such as ethylene and the formation of small aromatics, e.g., benzene and toluene, is described by a detailed chemical mechanism including 43 species and 304 elementary reactions, which is derived from the mechanism of Slavinskaya and Haidn [69]. Sub-mechanisms for kerosene combustion (16 species / 68 reactions) and formation of nitrogen oxides (17 species / 103 reactions) can optionally be added to the chemical model.

Only a brief description of the PAH and soot models is given here; more details are given in the works of Di Domenico *et al.* [70], and Blacha *et al.* [34]. Polycyclic aromatic hydrocarbons (PAHs) are discretized by three mass classes (bins) and described by a sectional approach. PAH chemistry is divided into four processes: PAH formation by interaction of the first PAH bin and gas phase, acetylene condensation, collisions between different PAH classes and PAH oxidation by hydroxyl (OH) and molecular oxygen (O₂).

Two modeling strategies for the evolution of the soot aerosol are followed. In the sectional soot approach developed by Blacha *et al.* [34], the size distribution of soot particles is discretized by 25 bins covering particle diameters from 1.3 nm to 329 nm. Since the computational cost of the sectional soot model is high (a separate transport equation must be solved for each bin), a two equation soot model developed by Di Domenico *et al.* [70], is frequently applied for simulations of complex combustion configurations, such as the model combustor addressed in this work. In two equation models, spherical soot particles and mono-disperse particle size distributions are assumed and soot is described by two independent variables, i. e., soot mass fraction and particle number density. Soot nucleation is modeled by PAH growth reactions involving the last PAH bin and soot surface growth is modeled by condensation of acetylene and PAHs onto the soot surface. Soot oxidation by OH and O₂ is taken into account. Coagulation is considered, using a collision frequency formulation, which is applicable to any Knudsen number regime. In order to demonstrate predictive capability, the soot model was validated for different laminar flames (Blacha *et al.* [34]) and a turbulent sooting jet flame (Köhler *et al.* [39]), where a good overall agreement was found using the same set of model constants for all test cases.

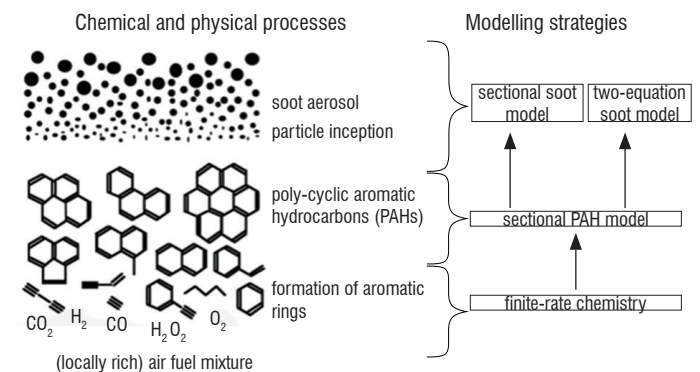


Figure 2 – Chemical and physical processes of soot evolution and corresponding modeling strategies followed by DLR

Experiments for the validation of the numerical strategies of pollutant prediction

The experimental validation of the numerical simulation of pollutant formation is a difficult task, because various issues must be considered: The accuracy of the pollutant prediction depends, on the one hand, on the detailed description of the physico-chemical phenomena triggering the pollutant formation and consumption and, on the other hand, on our ability to reproduce the main features of the turbulent flow. Another point is that we have to deal with different types of pollutants such as NO_x, soot, CO, UHC (Unburnt HydroCarbons), which have their own physics and/or chemistry. As the prediction of soot formation is generally considered to be more challenging than that of NO_x or CO, we focus here on the description of two experiments dedicated to the validation of numerical strategies to predict the soot formation in GT combustors. The first one has been performed by DLR and the second one by ONERA with the support of a DLR team for the soot measurements by laser-induced incandescence (LII).

DLR experiment

Burner setup

The objective of the DLR experiment is to reproduce some of the conditions encountered in gas turbine combustors (turbulence, swirl, increased pressure, secondary air injection), but to exclude the difficulties linked to the behavior of the liquid fuel phase. The burner described in more detail by Geigle *et al.* [41,42] is equipped with a dual swirl injector for a central and an annular air flow, which can be controlled separately, and a ring of tiny fuel nozzles injecting ethylene between both swirled air flows. At the exit of this injector, the flow is over stoichiometric on average, thus prompting soot formation in fuel-rich pockets. The combustor has a square cross section measuring 68 × 68 mm² with beveled edges and a length of 120 mm. Large combustion chamber windows measuring 127 × 59 mm² and thick pressure windows, both made of quartz, allow for good optical access; the former serve to maintain the high flame temperatures, the latter the pressure, which was increased up to 5 bar. Although the pressure can be much higher in GT combustors, already moderately increased pressure allows its effect on soot formation to be studied. 80 mm downstream from the main injector exit secondary air can be introduced through four pipes measuring 5 mm in diameter, fed through the four posts holding the combustion chamber windows. This secondary air injection is useful to study the oxidation of the soot particles formed in the upstream part of the burner. The exact geometry of the combustion chamber is shown in figure 3 and described by Geigle *et al.* [41-42].

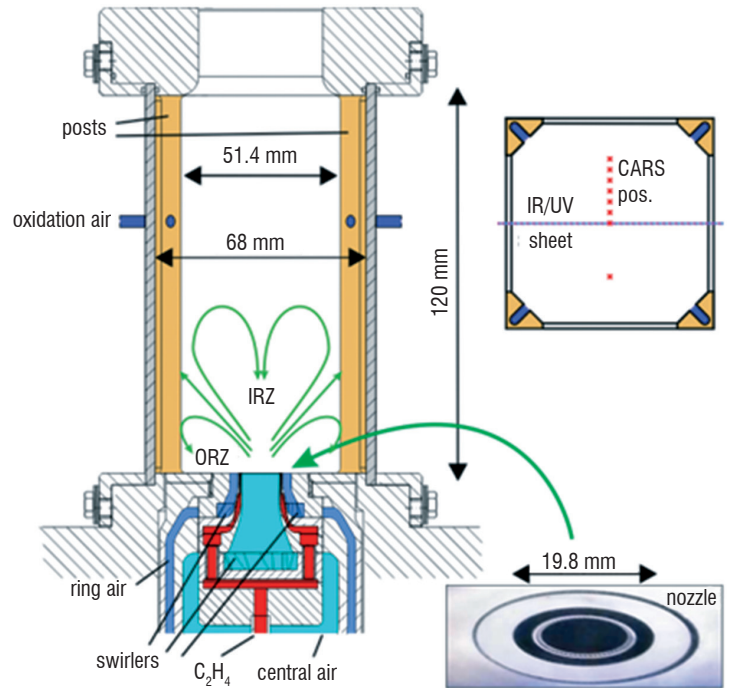


Figure 3 – Cross section of the DLR swirl burner operated with ethylene. The upper insert shows a horizontal cross-section at the height of the oxidation air inlets, as well as the locations of laser excitation for the diagnostics used

Laser-based diagnostics

A total of 16 operating points has been characterized by various laser diagnostic techniques, as presented in [41]. The suite of measurement techniques used consists of laser-induced incandescence (LII) for soot volume fraction distributions, laser-induced fluorescence (LIF) to determine OH and PAH distributions, shifted vibrational coherent anti-Stokes Raman scattering (SV-CARS) for temperature statistics and particle image velocimetry (PIV) (Geigle *et al.* [41-43], [71]). The challenging and/or time-consuming CARS and PIV techniques were only applied to a down-selection of operating conditions, while all flames are characterized by LII and LIF. The most comprehensive data set exists for the so-called reference flame at 3 bar and a primary equivalence ratio Φ of 1.2, which drops to 0.86 globally by addition of 40% oxidation air.

P [bar]	Φ	P_{primary} [kW]	$Q_{\text{air,c}}$ [slpm]	$Q_{\text{air,r}}$ [slpm]	Q_{fuel} [slpm]	Q_{oxi} [slpm]	$Q_{\text{air,c}}/Q_{\text{air}}$	$Q_{\text{oxi}}/Q_{\text{air}}$	Φ_{global}	P_{global} [kW]
3	1.2	32.2	140.8	328.5	39.3	187.4	0.3	0.4	0.86	38.6

Table 4 – Flame conditions of the reference flame used as a validation case within this publication: Pressure, p , mass flows for air through the burner (central and ring), $Q_{\text{air,c}}$ and $Q_{\text{air,r}}$, fuel, Q_{fuel} , oxidation air through secondary air inlets, Q_{oxi} , equivalence ratios, Φ , Φ_{global} , thermal powers, P , P_{global} and fractions $Q_{\text{air,c}}/Q_{\text{air}}$ and $Q_{\text{oxi}}/Q_{\text{air}}$ with $Q_{\text{air}} = Q_{\text{air,c}} + Q_{\text{air,r}}$. Flow rates are referenced to 1.013 bar and 273 K.

A detailed description of the diagnostic application is contained in the work by Geigle *et al.* [41–43], [71]. Therefore, only a short overview is provided here. For the quantitative soot volume fraction measurements obtained by Geigle *et al.* [41], a well-characterized laminar laboratory flame (Trottier *et al.* [72]) was inserted into the optical setup instead of the pressurized swirl flame, to serve as reference for the calibration of the LII signal to soot concentration. A homogeneous laser sheet with a height of 30 mm was used for the 1064 nm excitation of the LII signal recorded at 450 nm perpendicular to the excitation plane. For spatial correlation with OH and PAH LIF distributions, the LII laser sheet was expanded to 47 mm and an additional 90 mm high UV light sheet was introduced by a suitable dichroic mirror. For OH excitation, the UV laser was tuned to the $Q_1(8)$ line of the $A^2\Sigma-X^2\Pi(1,0)$ transition at $\lambda=283.55$ nm, PAH were excited slightly off-resonant of the OH transition, requiring higher pulse energies. The ultraviolet species emission was separated from the path of the LII signal by a suitable UV mirror and detected through a band pass filter centered around 315 nm (OH) or 300–400 nm (PAH); a temporal delay of both laser pulses with a duration of 400 ns was applied to temporally separate both effects. For PAH, the combination of excitation and detection wavelengths allows the monitoring of mainly small aromatic molecules consisting of two to four aromatic rings. Exemplary ensemble-averaged distributions are shown in figure 4. Figure 4a shows the OH distribution generated by the primary flame fed by combustion air and fuel; here, the additional oxidation air was switched off. Figs. 4b–4d display the reference flame conditions with oxidation air switched on. The OH distribution shows significantly increased OH levels in the center of the combustor, which is generated by the additional oxidation air when coming into contact with unburnt hydrocarbons surviving the primary reaction zone. The PAH distribution appears a bit higher in the flame, delayed by few millimeters. Further delayed relative to PAH, soot is visible in a V-shaped distribution. The central combustor remains soot-free due to the oxidative influence of the oxidation air, which is partly transported upstream into the inner recirculation zone, as visible by the significant OH signal levels. Instantaneous distributions show that small soot filaments fill the gaps left in the OH distributions between primary combustion and the OH generated by the oxidation air [42]. Simultaneous PAH/soot maps allow the identification of isolated PAH clouds, PAH transforming into soot and isolated, transported soot filaments [43].

The upstream influence of the oxidation air is also visible in the stereo PIV images in figure 5. These images were recorded upon dual-pulse excitation with 100 mm tall laser sheets at 532 nm. For acquisition, two cameras were mounted as close as possible to the pressure flange of the combustor to yield a stereoscopic viewing angle of approx. 37° . The non-reactive case (3 bar, $\Phi=1.2$, with oxidation air) is displayed in figure 5 left, clearly showing that the oxidation air is entrained upstream into the

inner recirculation zone. For the reference operating point at $\Phi=1.2$ under reactive conditions ensemble averaged velocities could be measured as a sum-of-correlation only due to the strong flame luminosity; replacing the initially used 10 nm bandwidth filter by a 2 nm filter provided a better suppression of soot luminosity, but resulted in a relatively small field of view due to its low transmission at non-perpendicular incident angles. A less sooting yet representative flame at $\Phi=0.9$ is shown as ensemble average of 1000 instantaneous images in figure 5 right.

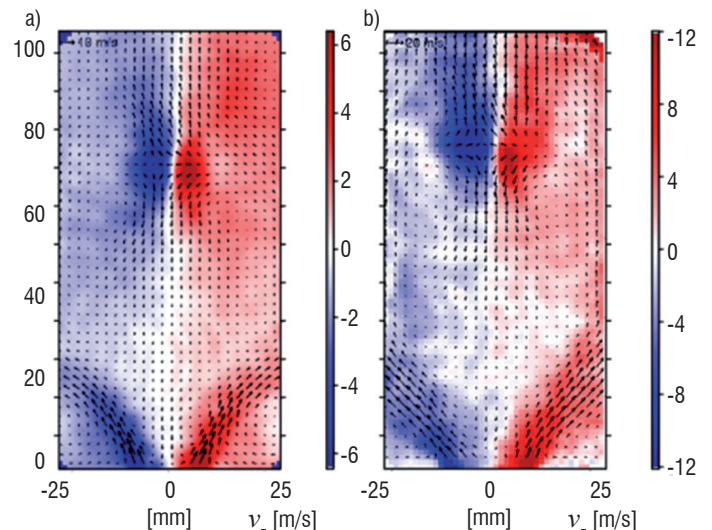


Figure 5 – Velocity fields of the non-reactive 3 bar case at $\Phi=1.2$ (left) and a leaner yet sooting and representative reactive case at $\Phi=0.9$ (right). Arrows show the in-plane velocity components, color represents the out-of-plane velocity

The application of CARS to the sooting swirl flames follows the approach presented by Tsurikov *et al.* [73]. Broadband N_2 vibrational CARS was applied in a folded BOXCARs configuration with excitation of the CARS signal by focusing and overlapping two narrowband laser beams at $\lambda=582$ nm and one broadband laser beam at $\lambda\approx 685$ nm. The measurement volume was determined to be 1.6 mm long and $300\ \mu\text{m}$ wide without flame. Figure 4d shows the measurement locations in the reference flame, figure 6 shows exemplary temperature statistics in the position on the axis where the oxidation air jets meet (a) and low in the inner recirculation zone (b). This type of temperature statistics, acquired at multiple locations in the flame, is highly valuable for model validation, as soot formation and oxidation strongly depend on local temperature.

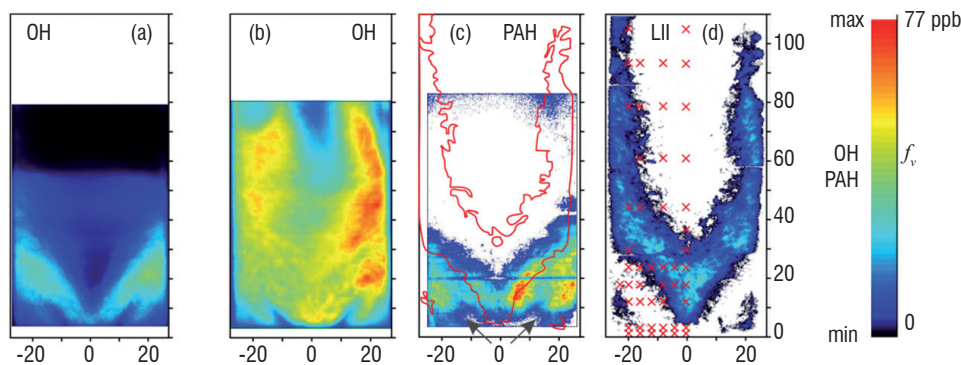


Figure 4 – Species distributions in reference flame (b) OH, (c) PAH, (d) soot. Without oxidation air injection (a) the OH distribution remains located at the bottom of the combustor; (c) also contains a contour of the soot distribution from (d), (d) shows labels where temperature statistics were measured by CARS

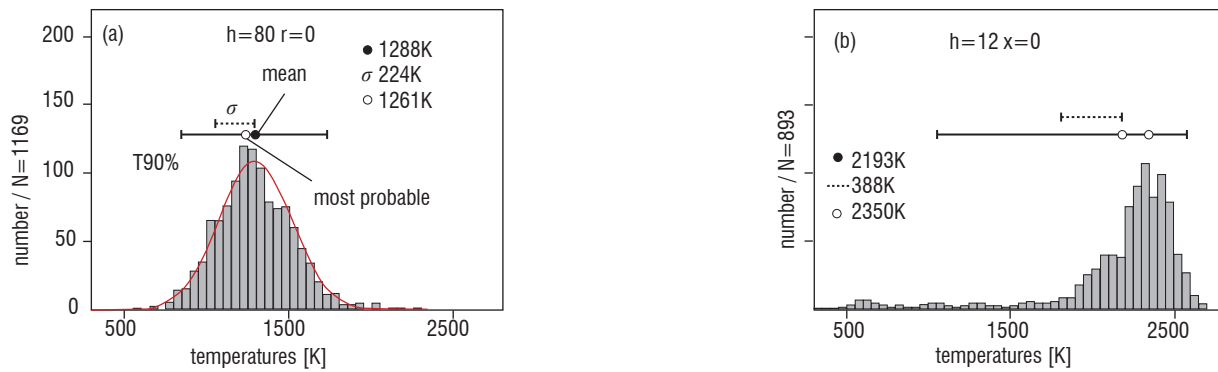


Figure 6 – Temperature statistics in the reference flame (a) at the stagnation point where the oxidation air jets meet and (b) low in the inner recirculation zone. The plots show mean and most probable temperatures and the width of the distribution, either as a range covering 90% of the instantaneous temperatures or as a width of a Gauss distribution where suited (dotted)

ONERA-SNECMA TLC experiment

The TLC experiment has been performed in the M1 facility of ONERA (see Cochet *et al.* [74]) within the framework of the TLC FP6 project [75] coordinated by Snecma Moteurs, known today as Safran Snecma. This experiment is aimed at providing a deep insight into a reactive flow subjected to conditions very close to those of a real aircraft gas turbine. It involves a single low NOx air-fuel injector feeding a combustor with a $105 \times 105 \text{ mm}^2$ cross-section equipped with lateral visualization windows. The liquid fuel is introduced on the one hand through a pilot injector and on the other hand through a multi-hole device in proportions that vary according to the flight regime: at low power most of the fuel is introduced through the pilot in order to obtain stable combustion, whereas at high power multi-hole injection is used in order to minimize NOx emissions. At the end of the combustion chamber, a nozzle with adjustable cross-section serves to vary the pressure between 4 and 20 bar. 4 sets of experimental conditions corresponding to the taxi, approach, climb and cruise regimes respectively, have been considered. Each set has its own pressure, inlet air temperature, pilot/multi-hole distribution and FAR (Fuel Air Ratio). Figure 7 displays the configuration of the TLC experiment. Note on the right part of the figure the arm crossing the flow upstream of the exit nozzle: This arm is used for gas sampling followed by exhaust gas analysis.

All of the air used for combustion goes through a swirler in the air-fuel injector in order to give a strong swirl to the reactive flow. Figure 8 shows the configuration of the injector.

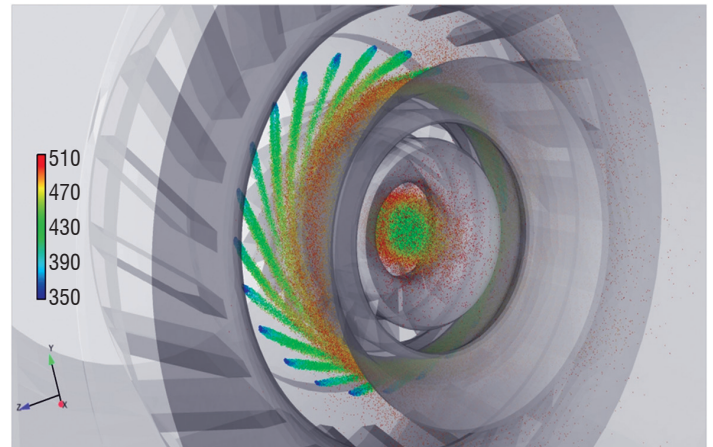


Figure 8 – Low NOx injector configuration; the colored part corresponds to simulated fuel droplets injected through the pilot (on the axis) and multi-hole devices (periphery); the color denotes the droplet surface temperature (scale in K)

In order to characterize the liquid phase PDA (Particle Doppler Anemometry), measurements have been carried out. They provide the early size and velocity distributions of the fuel droplets. These measurements are very useful to set the inlet conditions of the liquid phase in the calculation, because the simulation of the primary atomization is still out of reach in such semi-industrial cases. In order to locate the area where fuel evaporation and combustion take place LIF (Laser Induced Fluorescence)

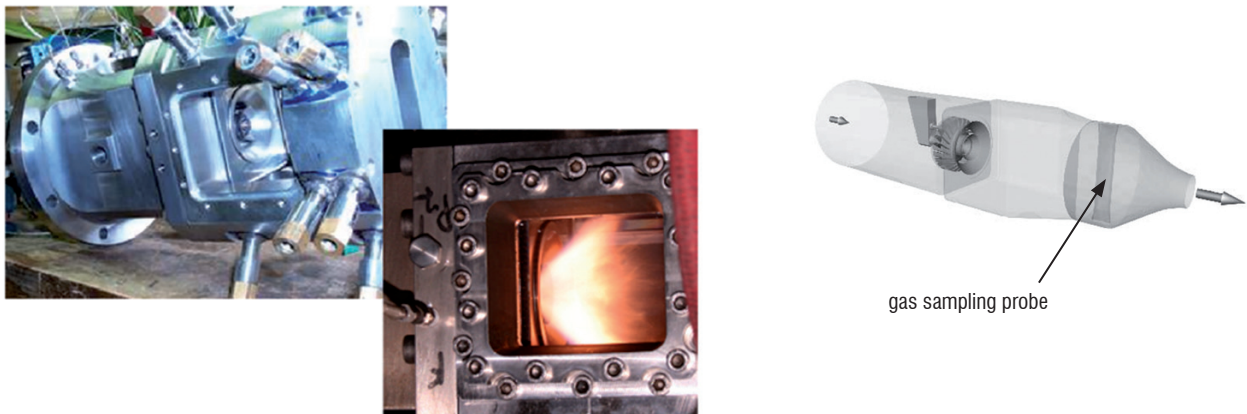


Figure 7 – Lateral view of the TLC combustor without and with combustion (left), schematic view of the TLC set-up with its downstream part including gas sampling probe and exit nozzle (right)

visualizations based on species resulting from fuel vaporization (mainly aromatics) and on the OH radical have been performed. Figure 9, extracted from the work of Orain *et al.* [76], shows that fuel evaporation takes place in a conical, v-shaped region located just downstream from the injector and that combustion, characterized by the presence of the OH radical (right), appears immediately downstream from the fuel evaporation in the shape of a very open cone, the upstream edge of which is attached to the injector.

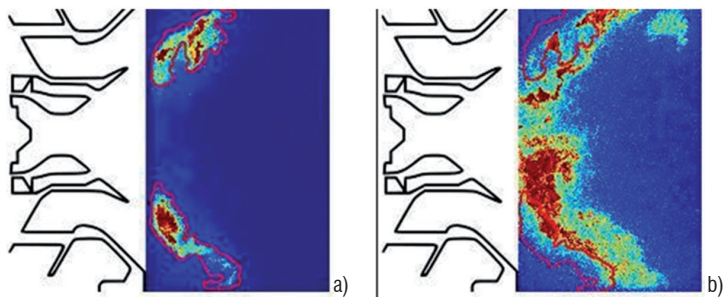


Figure 9 – Instantaneous LIF visualization of the fuel vapor (left, A), and of the OH radical (right, B); the same purple contour lines enclose the fuel vapor area on the left and right parts of the figure

Temperature is a crucial parameter because it greatly influences the features of the average flow, as well as the rate of pollutant formation. Temperature measurements by CARS have been achieved along 4 vertical lines crossing the combustor axis and situated respectively 20 mm, 29 mm, 51 mm and 65 mm downstream from the injector exit. Figure 10 shows the temperature profiles obtained for operating pressures of 4 and 19.5 bar in the last measurement cross-section.

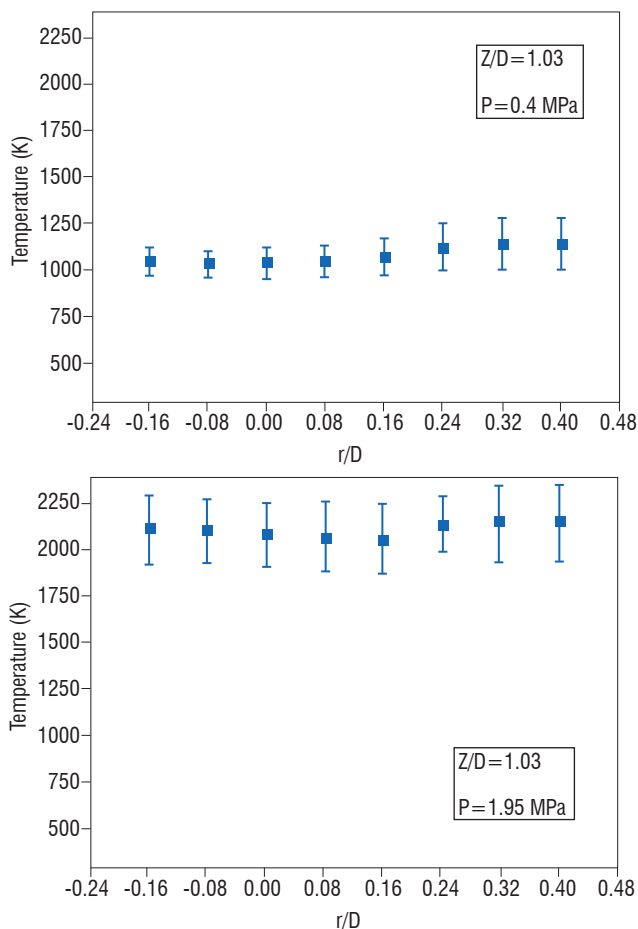


Figure 10 – Temperature profiles 65 mm downstream from the injector exit at 4 bar (left) and 19.5 bar (right) (abscissa: cross-coordinate r divided by $D = 64$ mm)

It can be noticed that these profiles are quite flat. This indicates a good quality of mixing in the central recirculation induced by the swirled injection. The temperature is much higher at high pressure because the FAR is larger at 19 bar (2.7 %) than at 4 bar (1.35 %).

A DLR team achieved LII measurements of soot in the TLC burner in the ONERA M1 facility for the 4 sets of experimental conditions [77]. Figure 11 shows the soot volume fraction field obtained for approach flight conditions (pressure of 9.5 bar), which are the most favorable to soot formation, knowing that take-off conditions are not inducing the highest rate of soot formation when a multi-hole injector is used.

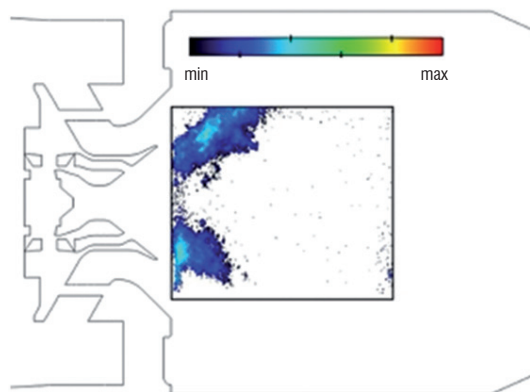


Figure 11 – Soot volume fraction field obtained by LII under approach flight conditions (arbitrary scale)

The emissions of other pollutants, such as NO_x, CO, UHC were measured by various gas analyzers after sampling at the outlet of the combustor. These analyzers gave us the emission index of each pollutant, i. e., the quantity of pollutant created for a given quantity of fuel injected in the combustor. For example, the NO_x emission index is 2.3 g of NO_x per kg of fuel for approach flight conditions.

All of these measurements and visualizations make up a set of data that are very valuable for the validation of numerical simulations. This experiment is complementary to that performed at DLR: After the validation step based on the DLR experiment in the case of gaseous fuel, the TLC experiment enables us to check that the model describing the fuel vaporization is adequately coupled with the combustion and pollutant formation models. Note that the set of data will be considered as complete only after achievement of the PIV (Particle Imaging Velocimetry) campaigns that are planned for the TLC experiments: The knowledge of the velocity field is of great importance for the validation of the simulations.

Calculation of the DLR burner for validation purposes

ONERA simulation

The DLR experiment described in section "DLR experiment" has been selected to test our numerical strategy for soot prediction. Figure 12 shows a schematic view of the DLR burner and the associated upstream plenum in which injection of primary air and ethylene is prepared. The square and round sections correspond to the burner and plenum respectively. The swirled injection is located between the plenum and the burner. The four pipes connected to the second half of the burner correspond to secondary air injection aimed at oxidizing soot.

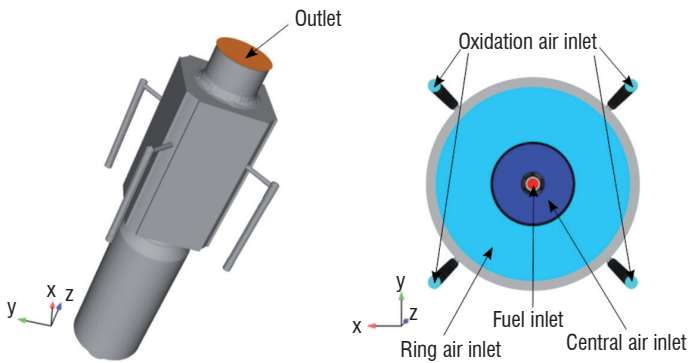


Figure 12 – The DLR burner: left, overall view of the burner and the plenum that supplies the injector; right, fluid supplies inside and beside the plenum upstream of the swirlers

The computational domain, shown in figure 13, includes a small part of the plenum, the swirled injection, the burner with the four injection sections for secondary air and a large open volume downstream from the combustor introduced to damp acoustic waves. The overall calculation grid is made up of 12.8 M tetrahedral cells. In order to take advantage of parallel processing the calculation grid has been divided into 256 parts distributed over the same number of processor cores. For the spatial discretization a MUSCL scheme of order 2 with a Roe type flux decomposition and a Van Leer type limiter is used. The time integration is implicit, which enables a relatively large time step of 10^{-6} s.

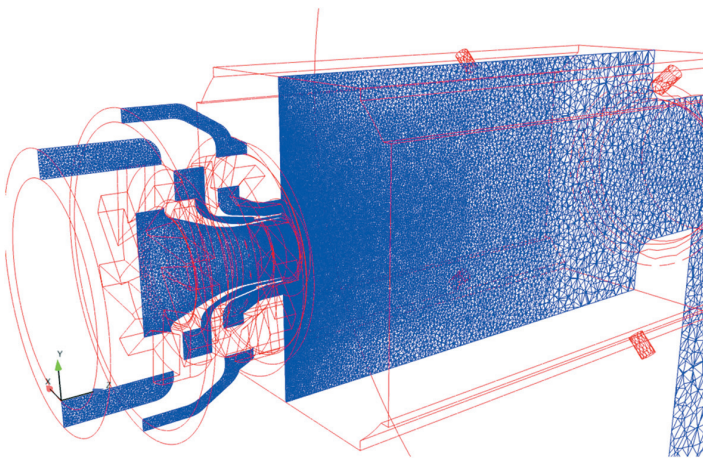


Figure 13 – Axial cut of the calculation grid

For the calculation, the case at 3 bar with secondary air injection has been selected among the 16 operating conditions studied [41]. As indicated in table 4, the global power of the burner is 38.6 kW and the equivalence ratio is 1.2 before dilution by secondary air and 0.86 after dilution. The injected volume flow rates from table 4 are translated in mass flow in table 5.

Boundary	Value
Central air inlet	3.020 g/s
Ring air inlet	7.047 g/s
Oxidation air inlet	4.020 g/s
Fuel inlet	0.818 g/s

Table 5 – Injection flow rates

On the burner walls, the following temperatures are imposed. The temperature is equal to 700 K on the lateral walls and 500 K on the wall orthogonal to the axis in the injection section.

Figure 14 shows instantaneous and time-averaged temperature fields obtained by the calculation. Hot gases are recirculated back to the injector by the central recirculation induced by the swirl and can be found inside the injector. A possible explanation of this phenomenon is that the internal injector surfaces have been considered as adiabatic, so the decrease in the gas temperature inside the injector can be underestimated. The zone of lower temperature around the axis in the second half of the burner is a result of secondary air injection.

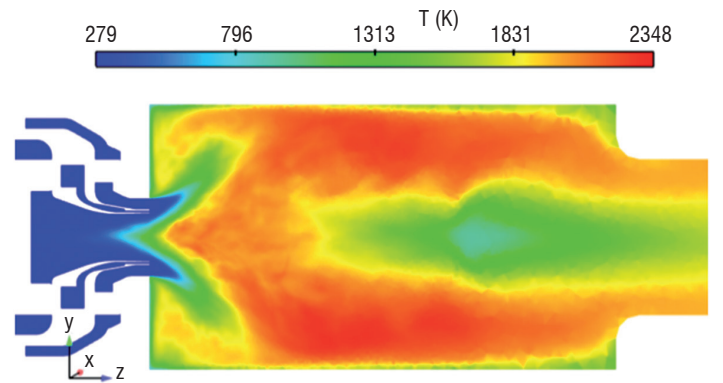
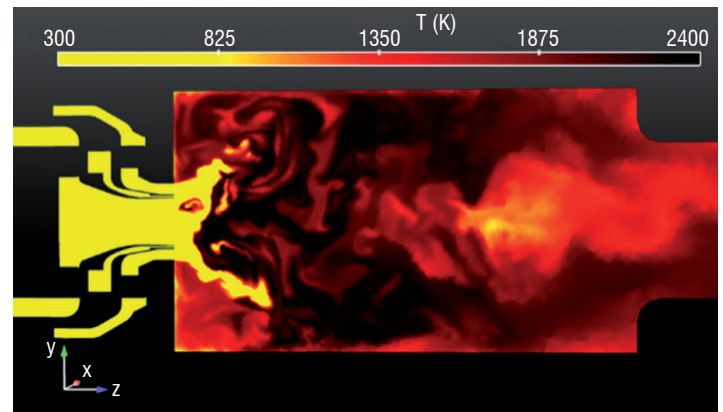


Figure 14 – Calculated instantaneous temperature field (top); averaged temperature field (bottom)

Temperatures obtained by averaging the LES calculation and those obtained experimentally by CARS are compared in figure 15. In the three profiles located near the inlet of the chamber (within the first three millimeters) we note that CARS measurements do not determine hot gases in the center of the injector, unlike the simulation, which gives a temperature of about 1000 K on the axis in the section $x=3$ mm. As mentioned previously, the presence of hot gases may be induced by non-adequate thermal boundary conditions inside the injector. However, since soot precursors such as acetylene are produced much further downstream, the discrepancy in the injection section has no influence on the soot formation. Despite an overestimation of the temperature for x between 12 and 24 mm, the agreement between measurements and simulation in cross-sections where the soot formation and oxidation are present is quite satisfactory. The simulation of soot formation can therefore be carried out with relative confidence concerning the temperature dependence of the source terms given by the Leung model.

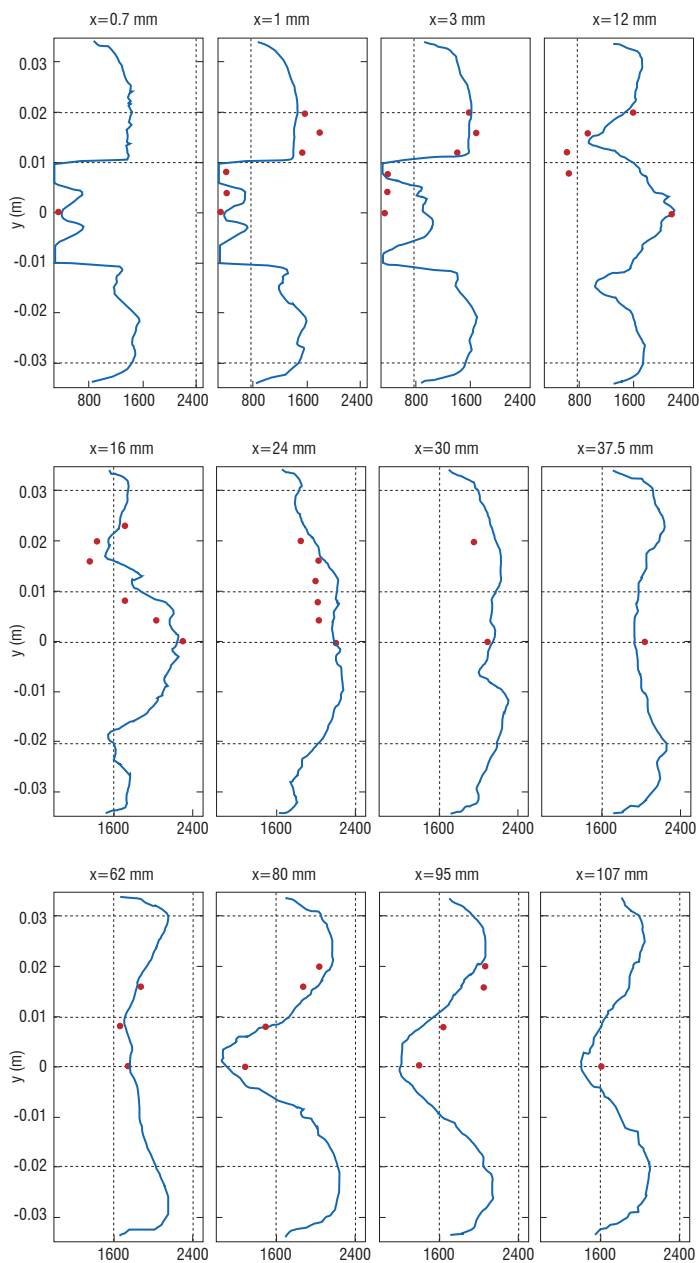


Figure 15 – Continuous lines: temperature profiles obtained by LES averaging; discrete points: CARS temperature measurements. All temperatures are plotted in K, x is the distance from the inlet section

Figure 16 shows, for a lengthwise cross-section, the map of the soot volume fraction obtained by the averaging of the LES calculation and the map resulting from time-averaging of the LII measurements. In this figure, the burner axis is vertical and the injection occurs at the bottom. The domain shown in the right part of the figure corresponds to the optically accessible regions of the combustor.

It appears that the calculation quite correctly reproduces the shape of the soot volume fraction distribution with soot formation in a conical region located downstream from the injector and the presence of soot near the walls further downstream. However, in the simulation, unlike in the experiment, the presence of soot does not extend as far as the end of the combustor. This indicates that the soot oxidation is too fast in the simulation and must be investigated further in future work. It can be noted that in both the calculation and the experiment soot is not present on the axis in the last two thirds of the burner: The secondary air penetrating deeply towards the combustor axis and partly recirculating upstream induces the complete oxidation of

soot particles, or even prevents their formation in a large area around the burner axis. Another point to be noticed is that the absolute level of the soot volume fraction, of the order of a few hundredths of a ppm, is correctly reproduced by the calculation.

In view of these satisfactory results, our methodology has been applied to the TLC burner quite representative of the conditions encountered in GT combustors.

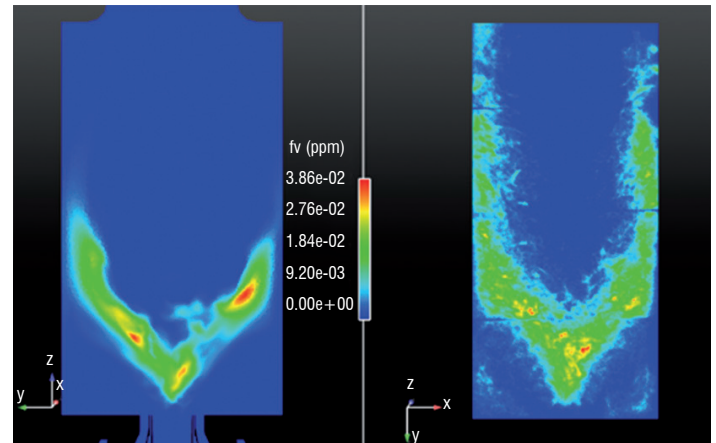


Figure 16 – Soot volume fraction in a lengthwise cross-section of the burner; left, averaged LES; right, LII time-averaged measurements

DLR simulation

Simulation Details

URANS simulations were performed on a 3D fully tetrahedral grid with 6.6 million points corresponding to 36.5 million tetrahedra. Inflow boundaries are placed well upstream of the swirlers. In order to take heat losses into account, isothermal walls are assumed. The estimated wall temperatures based on thermocouple measurements are 350 K for the swirlers, 600 K to 700 K for the combustion chamber and 900 K for the windows. Convective fluxes are discretized by a second-order upwind scheme, while a second-order central scheme is applied for diffusive fluxes. Time integration is carried out by a second-order backward differencing scheme. In order to ensure convergence, a time step width of $0.5 \mu\text{s}$ was applied.

Pressure-velocity coupling is performed by a projection method (Chorin [78]). Turbulence is treated by a two equation shear stress transport (SST) model (Menter [79]). A multivariate assumed probability density function (APDF) approach is used to close the chemistry turbulence interaction (Gerlinger [80]). The APDF approach is computationally efficient, since only two additional transport equations for the second order moments σ_T (temperature variance) and σ_Y (sum of species variances) are required. Heat radiation by soot is modeled by an optically thin approach (Di Domenico *et al.* [70]). In total, 57 transport equations are solved (five equations for momentum, pressure correction and specific enthalpy; two equations for turbulence modeling; 43 equations for gas phase species; five equations for PAHs and soot; and two equations for the second-order moments σ_T and σ_Y , respectively). Statistics were sampled over a physical time of 60 ms, which corresponds to approximately six flow-through times. The simulation took about 55 days on 256 cores (338000 CPU hours on Intel Xeon X5570 quad-core processors with a clock rate of 2.93 GHz).

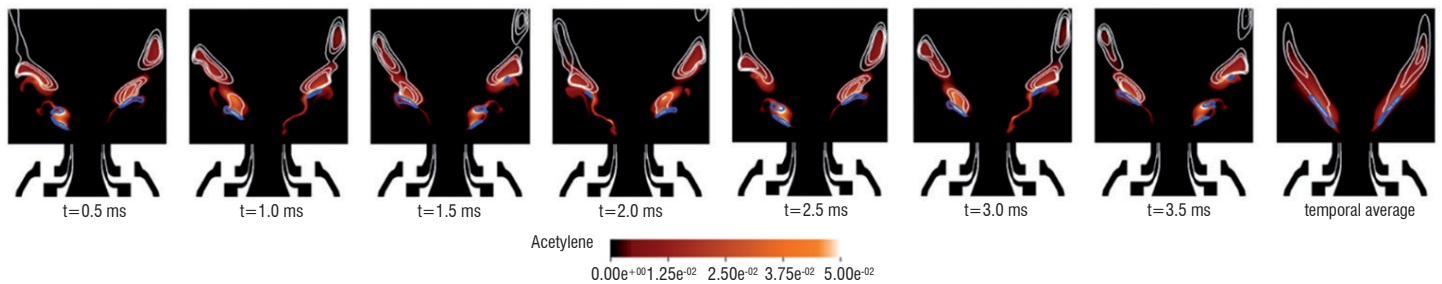


Figure 17 – Series of instantaneous and resulting time-averaged (right) distributions of calculated acetylene mass fractions as well as soot volume fraction isolines (white) and a PAH isoline (blue)

Motivation

The scope of this work is to investigate an efficient method (URANS, finite-rate chemistry with multivariate APDF source term closure and a two-equation soot model) for soot predictions under technically relevant conditions. It was shown in previous work (Eberle *et al.* [81]) that the time-averaged flame structure in terms of velocity field and temperature distribution is accurately predicted by this method, while some disagreement between the measured and predicted soot volume fraction f_v , in particular regarding the shape of the soot distribution, was observed. In contrast to URANS predictions, high soot concentrations were measured on the centerline of the flame. In this work, a time-resolved analysis is presented, providing detailed insight into soot evolution processes and showing the limitations of URANS for soot predictions under technically relevant conditions.

Soot inception and soot surface growth

In order to analyze soot nucleation and growth processes, distributions of acetylene are shown in figure 17 along with isolines of soot and PAH. PAH formation occurs in regions with high acetylene concentrations, since acetylene is a key species in the formation of the first aromatic ring, and small aromatics such as benzene and toluene are required for PAH formation. Conditions favorable for PAH formation are, for example, found at $t = 0.5$ ms in the left hand side flame wing in the vicinity of the injector, while, in contrast, not enough acetylene for PAH formation is present in the right hand side flame wing at $t = 1.0$ ms (the PAH structure observed further downstream was formed earlier).

Soot inception is modeled by PAH growth reactions, which involve the last PAH bin as reactant. Therefore, soot inception occurs only in regions where PAHs are present, for instance at $0.5 \text{ ms} < t < 1.0 \text{ ms}$ in the l.h.s flame wing or at $1.5 \text{ ms} < t < 2.0 \text{ ms}$ in the r.h.s flame wing. By tracking the respective PAH structures, it can be seen that PAHs contribute to further soot growth. Two pathways are possible: Soot inception or surface growth by condensation of PAHs on the soot surface. While regions with high PAH concentrations are small and spatially separated, large regions with high acetylene concentrations are observed. The maximum acetylene mass fraction is approximately five orders of magnitude higher than the maximum PAH mass fraction. By tracking the bottommost soot structure at $t = 0.5$ ms in the r.h.s flame wing, it can be seen that after the corresponding PAH structure is consumed at $1.5 \text{ ms} < t < 2.0 \text{ ms}$, acetylene continues to contribute to soot surface growth, until all acetylene in the vicinity of this soot structure is consumed at $t = 3.5$ ms. From $t = 3.5$ ms onwards, this soot structure is isolated from PAH and acetylene. In contrast to the measurements, no soot is predicted on the burner axis in the vicinity of the fuel injection. This discrepancy is attributed to the limitations of URANS as discussed below.

Unsteadiness and soot oxidation

In order to shed light on dominant unsteady motions and soot oxidation processes, distributions of the soot oxidants oxygen O_2 (left hand side) and OH (right hand side) are shown in figure 18 along with isolines of the soot volume fraction f_v . The narrow fuel jets are enveloped by the central and annular air jets. A periodic behavior with a frequency $f \approx 500$ Hz resembling a precessing vortex core is observed by tracking the O_2 mass fraction. At $t = 0.5$ ms a low penetration depth of the central air jet is observed, favoring rich combustion conditions and acetylene formation (see figure 17). The penetration depth of the central air then increases until the maximum is reached at $t = 1.5$ ms. At this time, the acetylene concentration is not sufficiently high for PAH production and consequently no new soot structures are formed. From $t = 1.5$ ms on, the penetration depth decreases until the minimum is reached again at $t = 2.5$ ms. At this time, high acetylene concentrations are found and PAHs are formed. Inception of new soot structures occurs between $t = 2.5$ ms and 3.0 ms.

At $t = 0.5$ ms, high O_2 concentrations might prevent soot from penetrating the outer recirculation zone. No significant interactions between oxygen and soot are observed further downstream, however. Soot oxidation by O_2 is thus not dominant in this test case. Soot oxidation by OH is discussed by tracking the soot structures present at $t = 0.5$ ms on the right hand side. The downstream soot structure (located above in the figure) is isolated from acetylene and PAHs at $t = 1.5$ ms and then, due to the subsequent absence of growth processes, oxidized by hydroxyl. At a given instance in space and time, soot and hydroxyl do not coexist due to the high oxidation rates. Unsteady simulations are thus required to properly resolve the correlation between hydroxyl and soot.

Geigle *et al.* [43] performed simultaneous measurements of OH and soot and found zones with low OH concentrations in the inner recirculation zone. These zones were filled with soot filaments. This is in contrast to URANS, which persistently predicts high OH concentrations in the cited region, thereby preventing the existence of soot due to the high oxidative potential of OH. The authors attribute the persistent prediction of hydroxyl to the limitations of URANS, which relies on statistically averaged equations and thus only resolves deterministic unsteady motions. Consequently the reproduction of concentration filaments seems difficult with URANS but Large-Eddy Simulations are expected to resolve the instantaneous hydroxyl distribution more accurately and to subsequently predict soot in this region with better agreement against measurements.

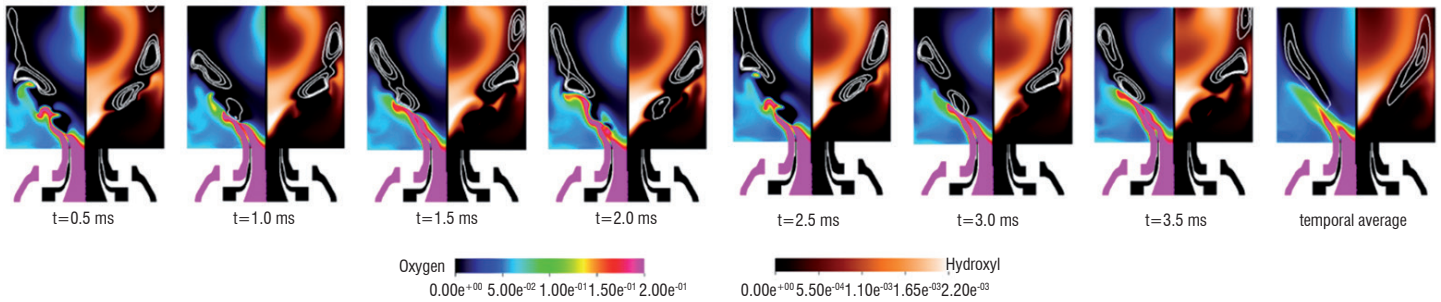


Figure 18 – Series of instantaneous and resulting time-averaged (right) distributions of calculated molecular oxygen (left hand side of the respective plot) and hydroxyl mass fractions (right hand side of the respective plot), as well as soot volume fraction isolines

Conclusions and outlook

URANS simulations of an aero-engine model combustor using finite-rate chemistry with a multi-variate assumed PDF source term closure and a two-equation soot model were successfully performed. A time-resolved analysis of soot evolution revealed that soot nucleation is influenced by a periodic unsteady motion at $f \approx 500$ Hz. In contrast to the measurements, URANS does persistently predict high hydroxyl concentrations on the central axis of the burner, which prevents soot presence in this region. Large-eddy simulations will be performed next, in order to better predict the instantaneous hydroxyl distribution and to subsequently obtain better agreement between the calculated and measured soot volume fraction. In the planned simulations, a sectional soot model will be used to obtain information regarding the particle size distributions.

ONERA calculation of the TLC combustor

Main features of the simulated turbulent reactive flow

This section presents the conditions and the main features of the ONERA simulation of the TLC combustor. The liquid kerosene is introduced for one part close to the combustor axis through a pilot injector creating a liquid hollow cone along the burner axis (pilot stage), and for another part into an annular flow of swirled combustion air through a set of small holes equally distributed over a ring normal to the burner axis (main stage). Considering that the use of liquid fuel can induce stronger mixture fluctuations, an assumed PDF $P(Z)$ of the mixture fraction Z is introduced in the calculation of the reaction rate, so that Eq. (5) is replaced by

$$Ra(x, r) \propto \frac{1}{T} \int p'(x, r, t) q'(x, r, t) dt \quad (7)$$

The computational domain, shown in figure 19, includes the plenum used to supply the injection, the TAPS injector, the combustor, the choked nozzle used to impose the required pressure in the combustor and a large open volume with large meshes to damp perturbations induced by acoustic waves traveling in the calculation domain when the low external pressure is recovered. Two calculation grids have been tested, one with 4 M tetrahedral cells, 2.1 M being assigned to the combustor, one with 10 M tetrahedral cells, 5 M being assigned to the combustor.

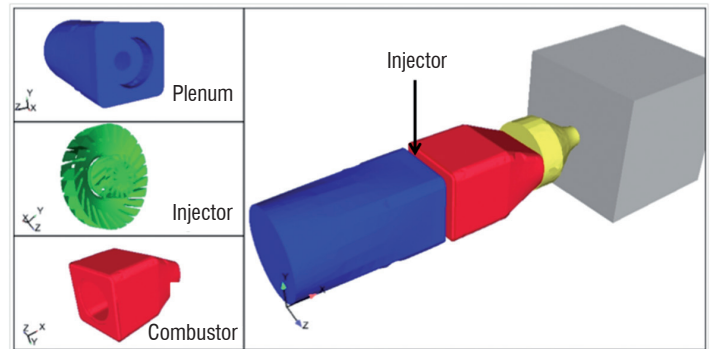


Figure 19 – Computation domain for the TLC calculation; plenum in blue, TAPS injector in green, combustor in red and choked nozzle in yellow

The operating conditions which are modeled are given in table 6. They correspond to an intermediate flight regime, which has been selected because the proportion of fuel injected through the pilot stage is relatively high (50 %). Thus, more soot is produced than at full power, for which a larger proportion of fuel is injected through the main stage. For combustion of the vaporized kerosene, the chemical kinetics of Luche *et al.* [82] is considered.

Condition	Value
<i>Air inlet MFR through TAPS injector (Mass Flow Rate)</i>	0.485 kg/s
<i>Total MFR of cooling air along walls</i>	0.232 kg/s
<i>Kerosene MFR main stage</i>	6.434 g/s (50 % of the total fuel MFR)
<i>Droplet diameter (single value)</i>	25 μm
<i>Kerosene MFR pilot stage</i>	6.434 g/s (50 % of the total fuel MFR)
<i>Droplet diameter (single value)</i>	15 μm
<i>Air inlet temperature</i>	592 K
<i>Lateral wall temperature</i>	700 K
<i>Other walls</i>	Adiabatic conditions
<i>Chamber pressure</i>	9.5 bar

Table 6 – Conditions of the TLC calculation

Before applying the above mentioned numerical strategy for soot prediction, a first calculation has been carried out with a simple combustion model (two step mechanism for kerosene oxidation) and a relatively coarse numerical grid made of 4 M cells. Some large discrepancies between the temperatures obtained by this calculation and the measured temperatures have been noted. Consequently, a more refined calculation grid including 10 M cells has been created and used for a new calculation achieved with the same simple combustion models. The refined grid greatly improved the numerical results, although the agreement on temperatures remained unsatisfactory. As the use of a larger grid was not possible for practical reasons, this grid of 10 M cells has been adopted to apply our numerical strategy for soot prediction. The use of a more sophisticated combustion model based on tabulated chemistry did not result in better agreement concerning the temperature.

Figure 20 shows the temperature field obtained numerically with tabulated chemistry and the grid of 10 M cells.

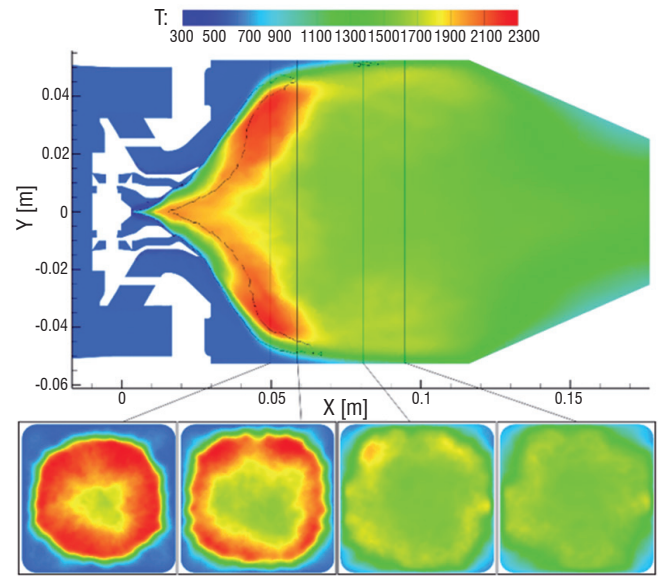


Figure 20 – Temperature field obtained numerically (temperatures in K); cross-section views are given for the four sections where CARS measurements have been performed

Figure 21 gives a comparison of the profiles of averaged temperature and temperature fluctuations obtained numerically and experimentally by CARS. BFER refers to the simple mechanism of kerosene oxidation, while FTC refers to the tabulated chemistry used to obtain the reaction terms of the main species and the concentration of the minor species involved in the soot formation or oxidation. The higher temperature obtained numerically in the recirculation induced by the injection swirl is difficult to explain: in Dorey [83], the CFD simulation was coupled with an accurate radiative transfer calculation using a Monte Carlo method, in order to take into account the radiative heat losses. Due

to the low soot volume fraction and the important reabsorption of the emitted radiation by the media, the decrease in temperature induced by the radiative heat loss is hardly greater than 20 K: this heat loss does not explain the difference (relative) to the experiment. Surprisingly, the agreement between experiment and simulation is much better for the fluctuations than for the averaged values.

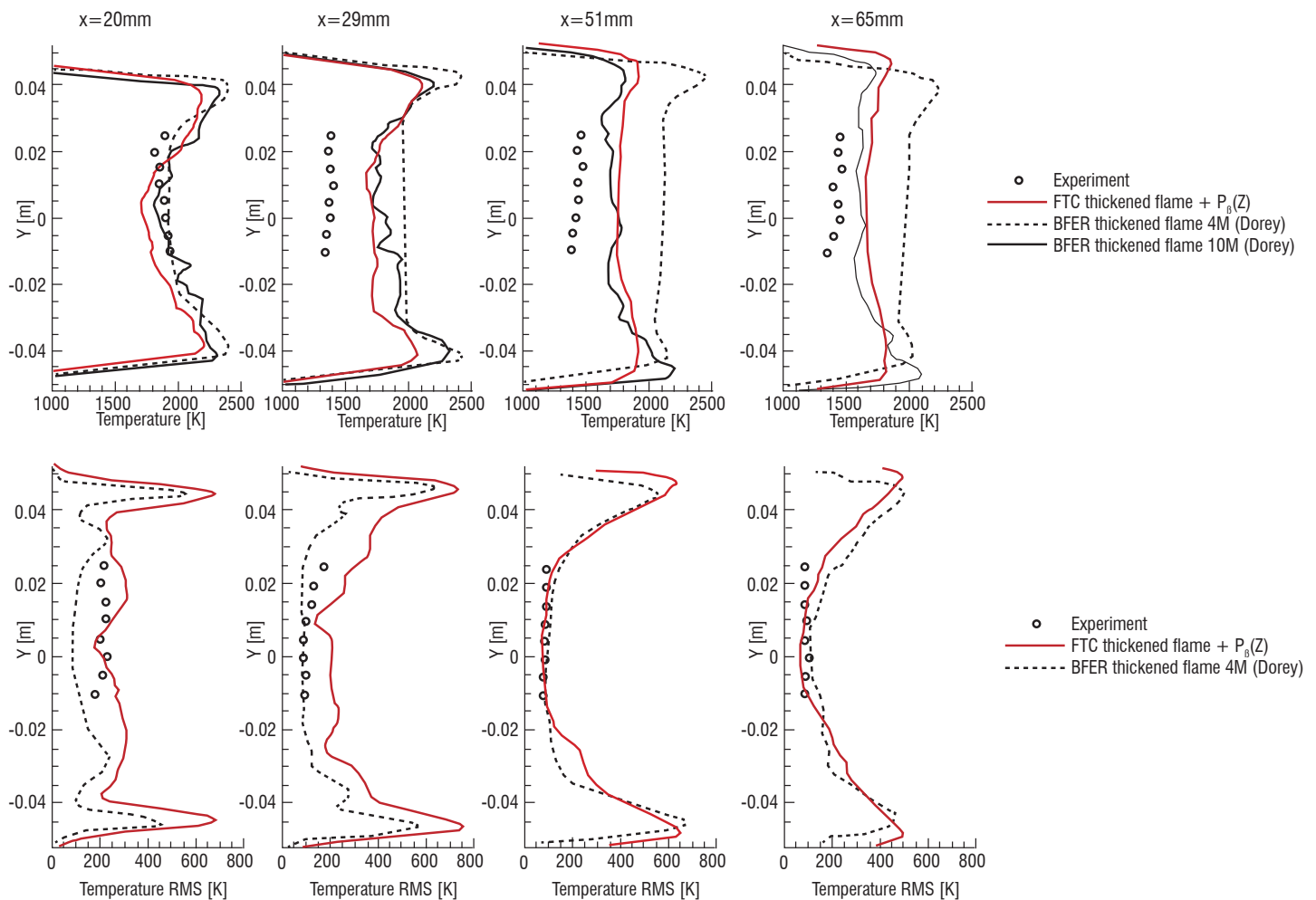


Figure 21 – Profiles of averaged temperature and temperature fluctuations obtained experimentally and numerically; temperature fluctuations have been evaluated only for the FTC calculation with 10 M cells and the BFER calculation with 4 M cells

Calculation of NOx emissions

Pollutants known as NOx are made up of the NO and NO₂ species, which are produced during combustion in small quantities compared to species resulting from the fuel oxidation. The tabulated chemistry described in section "Physical Models and Associated Numerical Methodology" gives access to minor species concentrations and therefore can be considered as an appropriate methodology to calculate NOx formation. However, implementation is far from trivial because NOx formation involves characteristic chemical times which are much larger than those of fuel oxidation. This means that the usual progress variable defined by Eq. (2) is not applicable to correctly discretize the NO mass fraction gradients in the chemical manifold, since a very small change in c can lead to a very large change in the NO mass fraction in the post-flame region. This problem can be addressed by including the NO mass fraction into the definition of the progress variable (Godel *et al.* [13], Boucher *et al.* [65]) or by transporting NO in the simulation instead of picking its concentration in the chemical table (Vreman *et al.* [64], van Oijen and de Goey [84]). As suggested by Van Oijen and De Goey [84], we have combined the two solutions: a transport equation is solved for the NO mass fraction and the variable progress is now defined, before normalization, as:

$$C = C_{init} + \kappa \frac{Y_{NO}}{M_{NO}} \quad (8)$$

where C_{init} is the initial non-normalized progress variable, κ is a non-dimensional constant, M_{NO} is the molar mass of NO and Y_{NO} is the NO mass fraction. The value of κ has been taken equal to 100 as recommended by Boucher *et al.* [65]. Other authors (van Oijen and de Goey [84]) recommend a higher value, but such a high value is necessary only when the NO mass fraction remains very small and barely impacts the value of C . The introduction of the NO₂ mass fraction into the progress variable is not necessary: given that the conversion of NO into NO₂ is relatively slow in the considered combustors, Eq. (8) leads to a monotonic evolution of C with the oxidation process.

The tabulated chemistry based on the kinetics of Luche *et al.* [82] used in our simulations includes both mechanisms of prompt and thermal NO formation. The approach combining the new definition of the progress variable and the transport equation for NO leads to the NO mass fraction field shown in figure 22.

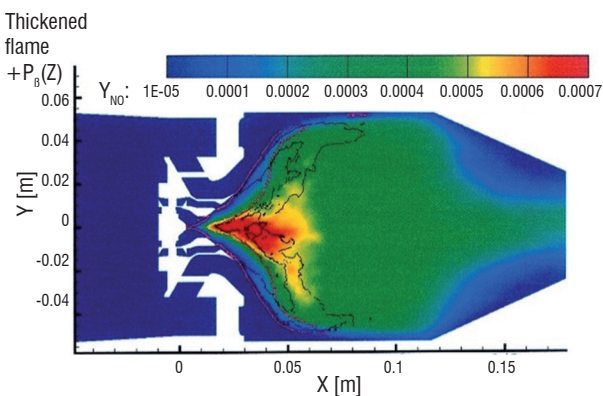


Figure 22 – NO mass fraction field in the lengthwise mid-plane

The high mass fraction observed in the conical part of the central recirculation results from high temperatures and a large residence time. Near the outlet section, the NO mass fraction is lower because most of the gas mixture reaching the combustor exit bypasses the central recirculation, thus avoiding a large residence time and high temperatures.

Strictly speaking, the tabulated chemistry approach used in these simulations is designed for premixed combustion and, even though the low NOx injector of the TLC combustor generates quite good mixing between fuel and air, not all of the combustion occurs in the regime of a perfectly premixed flame. However, it was checked by Boucher (see Figs. 11.23 and 11.24 of [85]) that the largest proportion of the combustion is of a premixed or partially premixed type and thus can be tackled by the tabulated chemistry approach. The emission indices for NO and NOx measured by gas sampling at the outlet of the combustor are 0.9 and 2.3 g/kg of fuel, respectively. The corresponding indices obtained by the simulation are 5.6 and 9.3 g/kg of fuel, respectively. This discrepancy between experiment and simulation is fully coherent with the results of section "ONERA Simulation" for the temperature: the effort made at this stage did not enable us to obtain a satisfactory agreement for temperatures in the core of the main recirculation zone. Considering the strong dependence of the NO reaction rate on temperature, it is not surprising that the simulation overestimates NO and NOx formation. Despite the significant deviations between simulation and experiment, we evaluate this result to be interesting because it perfectly illustrates that the prediction of pollutant formation requires not only a physical model accurately describing the evolution of pollutant species in a given thermo-chemical environment, but also a highly accurate reproduction of the main features of the reactive flow. The next step of work will be to improve the temperature prediction by paying an additional CPU effort into grid refinement. Planned velocity measurements will be also of great help to analyze the results, specifically potential sources for deviations of the temperatures, in greater detail.

Calculation of the soot mass fraction field

Despite the deficit of temperature prediction, the Leung model has been used with the FTC approach to calculate soot formation. The fields of the C₂H₂ (soot precursor) mass fraction and soot volume fraction are given in figure 23.

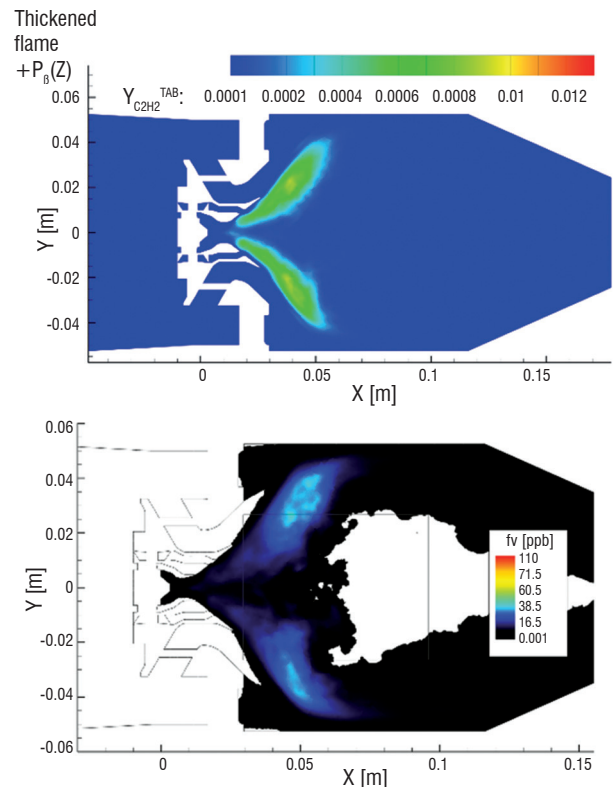


Figure 23 – Fields of the C₂H₂ mass fraction (top) and soot volume fraction (bottom) obtained numerically

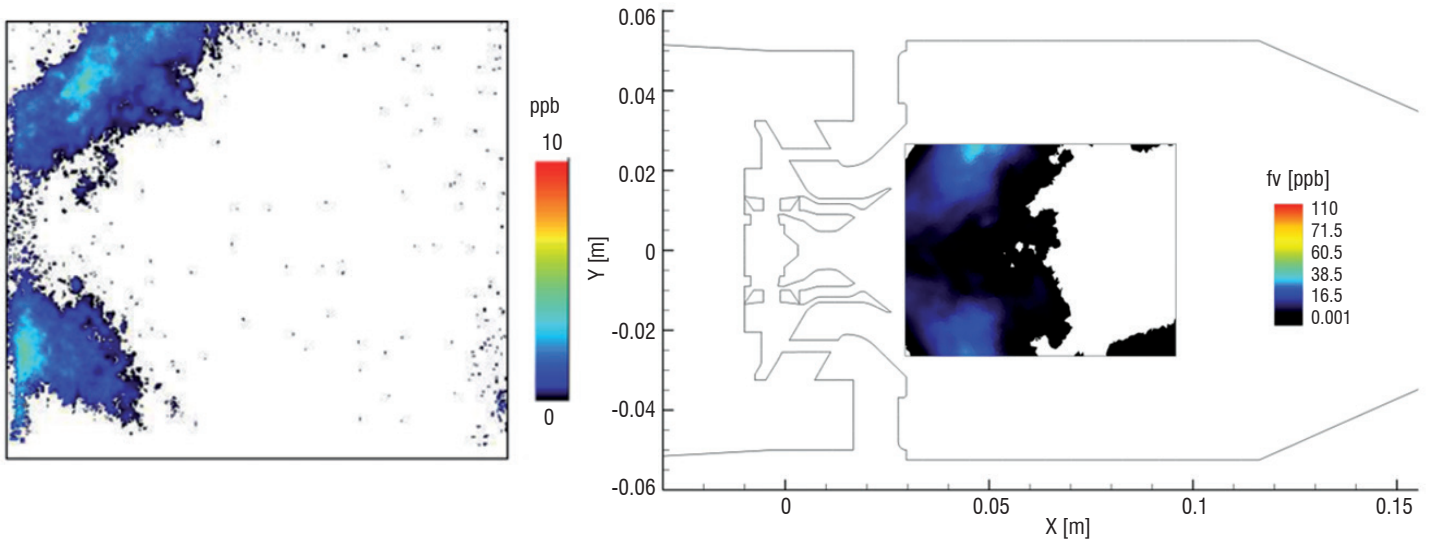


Figure 24 – Soot volume fraction obtained by LII (left) and by the calculation (right); the window shown in the calculated map corresponds to the measurement window displayed on the left

As for the DLR burner, soot is located in an open conical region, which does not extend very far downstream. However, unlike the DLR burner, soot is not present close to the wall because air cooling films are introduced along the lateral walls, i.e., combustor windows. The soot volume fraction map is slightly shifted downstream compared to the C_2H_2 mass fraction distribution. The numerical results concerning soot are compared to LII measurements in figure 24.

The shapes of the soot distributions obtained experimentally and numerically are similar, with a high soot volume fraction in the conical region located immediately downstream of the injection bowl and no soot on the axis of the combustor where the central recirculation of hot gases induced by the swirl takes place. The quantitative level of the soot volume fraction is however overestimated by an order of magnitude (factor 10) in the calculation. As for the NO and NOx indices, the overprediction of temperature is likely to be the reason for this discrepancy. Another point to emphasize is that all soot is oxidized before the outlet of the combustor, as shown in figure 9. This is in agreement with the sampling measurements made at the outlet of the combustor, which do not detect soot even at a level significantly below LII values. A calculation test made with the rough soot model of Magnussen gives quite good results in the region of the measurement window, but does not exhibit complete oxidation of the soot particles so a non-negligible amount of soot is found at the combustor outlet. This is not in agreement with the sampling measurements and validates our preference for the Leung model.

Conclusion

Examples of numerical strategies and associated validation experiments for the numerical prediction of pollutant formation in gas turbine combustors have been presented. The prediction of pollutant formation in complex turbulent reactive flows typical for GT combustors

is a challenging task. To date, there is no solution to perfectly solve the problem at a moderate CPU cost. Therefore, a compromise must be found between the complexity of the physico-chemical model for pollutants and the description of the turbulent reactive flow fixing the parameters of the pollutant model. For soot prediction, two strategies have been proposed: the first one initiated by ONERA is based on the simple soot model of Leung *et al.* and emphasizes the unsteady description of the turbulent reactive flow; the other one initiated by DLR is based on a soot model with more physics, but investing less effort on the flow description. Both strategies lead to quite satisfactory results concerning the simulation of the semi-technical scale DLR experiment. The first one works with a soot model, which is less CPU consuming, but the second one can be applied to more general configurations without adjusting the soot model. A strategy was also proposed for the prediction of NOx. The discrepancy between simulation and experiment obtained when this strategy was applied to the TLC combustor confirms that the prediction of NOx essentially requires a correct prediction of the local temperature field.

The numerical strategies for pollutant prediction and the involved physical models must be carefully validated. Many laminar experiments can be found in literature to validate the basis of physical models, but experiments allowing for validation of the coupling between these physical models and the calculation of the turbulent reactive flow transporting the pollutants are less common. We have presented two different experiments, the first one at the semi-technical scale achieved by DLR, the second one at the technical scale achieved by ONERA with the participation of DLR for the soot measurements. The first one provides a deep insight into the process of soot formation, with valuable information on the influence of the dilution air injection on soot oxidation; the second one accurately reproduced the running conditions of a GT combustor, in particular the injection of liquid fuel through a low NOx injector. However, the second data set will have to be completed by gas velocity measurements ■

References

- [1] M. RALPH and S. BAKER – *Aircraft Technology Improvements, Icao Technology Goals for Nox Second Independent Expert Review*. ICAO environmental report, Chapter 2, 2010.
- [2] ICAO – *Environmental Protection*. Annex 16, Volume II, 2008.
- [3] J. DELHAY, P. DESGROUX, E. THERSSEN, H. BLADH, P.-E. BENGTSOON, H. HÖNEN, J. D. BLACK and I. VALLET – *Soot Volume Fraction Measurements in Aero-Engine Exhausts Using Extinction-Calibrated Backward Laser-Induced Incandescence*. Appl. Phys. B, 95(2009):825-838, 2009.
- [4] J. D. BLACK and M. P. JOHNSON – *In-Situ Laser-Induced Incandescence of Soot in an Aero-Engine Exhaust: Comparison with Certification Style Measurements*. Aerosp. Sci. Technol. 14 (2010):329-337, 2010.
- [5] A. PETZOLD, R. MARSH, M. JOHNSON, M. MILLER, Y. SEVCENCO, D. DELHAYE, A. IBRAHIM, P. WILLIAMS, H. BAUER, A. CRAYFORD, W. D. BACHALO and D. RAPER – *Evaluation of Methods for Measuring Particulate Matter Emissions from Gas Turbines*. Environ. Sci. Technol., 45,8(2011):3562-3568, 2011.
- [6] J. M. COHEN, N. M. REY, C. A. JACOBSON and T. J. ANDERSON – *Active Control of Combustion Instability in a Liquid-Fueled Low Nox Combustor*. Gas Turbine and Aeroengine Congress and Exhibition, Stockholm, Sweden, June 2-5, 1998.
- [7] T. C. LIEUWEN – *Experimental Investigation of Limit-Cycle Oscillations in an Unstable Gas Turbine Combustor*. J. Prop. Power, 18,1(2002):61-67, 2002.
- [8] A. S. FEITELBERG and M. A. LACEY – *The GE Rich-Quench-Lean Gas Turbine Combustor*. J. Eng. Gas Turbines Power 120,3(1998):502-508, 1998.
- [9] V. JERMAKIAN, V. G. MCDONELL and G. S. SAMUELSEN – *Experimental Study of the Effects of Elevated Pressure and Temperature on Jet Mixing and Emissions in an RQL Combustor for Stable, Efficient and Low Emissions Gas Turbine Applications*. Advanced Power and Energy Program, University of California, Irvine <http://www.energy.ca.gov/2012publications/CEC-500-2012-001/CEC-500-2012-001.pdf>, 2012.
- [10] R. STICKLES and J. BARRETT – *TAPS II Technology, Final Report*. Technology Assessment, Open Report FAA, Continuous Lower Energy, Emissions and Noise, (CLEEN) Technologies Development, http://www.faa.gov/about/office_org/headquarters_offices/apl/research/aircraft_technology/cleen/reports/media/TAPS_II_Public_Final_Report.pdf, 2013.
- [11] E. RIESMEIER, S. HONNET and N. PETERS – *Flamelet Modeling of Pollutant Formation in a Gas Turbine Combustion Chamber Using Detailed Chemistry for a Kerosene Model Fuel*. J. Eng. Gas Turbines Power, 126(2004):899-905, 2004.
- [12] P. SCHMITT, T. POINSOT, B. SCHUERMANS and K. P. GEIGLE – *Large-Eddy Simulation and Experimental Study of Heat Transfer, Nitric Oxide Emissions and Combustion Instability in a Swirled Turbulent High-Pressure Burner*. J. Fluid Mech., 570(2007):17-46, 2007.
- [13] G. GODEL, P. DOMINGO and L. VERVISCH – *Tabulation of Nox Chemistry for Large-Eddy Simulation of Non-Premixed Turbulent Flames*. Proc. Combust. Inst., 32(2009):1555-1561, 2009.
- [14] M. ILBAS, I. YILMAZ and Y. KAPLAN – *Investigations of Hydrogen and Hydrogen-Hydrocarbon Composite Fuel Combustion And Nox Emission Characteristics in a Model Combustor*. Int. J. of Hydrogen Energy, 30:1139-1147, 2005.
- [15] M. J. LANDMAN, M. A. F. DERKSEN and J. B. W. KOK – *Effect of Combustion Air Dilution by Water Vapor or Nitrogen on Nox Emission in a Premixed Turbulent Natural Gas Flame: an Experimental Study*. Combust. Sci. Tech., 178: 623-634, 2006.
- [16] S. C. LI and F. A. WILLIAMS – *NOx Formation in Two-Stage Methane-Air Flames*. Combust. Flame, 118(1999):399-414, 1999.
- [17] L. K. SZE, C. S. CHEUNG and C. W. LEUNG – *Appearance, Temperature, and NOx Emission of Two Inverse Diffusion Flames with Different Port Design*. Combust. Flame, 144(2006):237-248, 2006.
- [18] W. MEIER, A. O. VYRODOV, V. BERGMANN and W. STRICKER – *Simultaneous Raman/Lif Measurements of Major Species and NO in Turbulent H₂/Air Diffusion Flames*. Appl. Phys. B, 63:79-90, 1996.
- [19] V. SICK, F. HILDENBRAND and P. LINDSTEDT – *Quantitative Laser-Based Measurements and Detailed Chemical Kinetic Modeling of Nitric Oxide Concentrations in Methane-Air Counterflow Diffusion Flames*. Proc. Combust. Inst., 27(1998):1401-1409, 1998.
- [20] W. MEIER, R. S. BARLOW, Y.-L. CHEN and J.-Y. CHEN – *Raman/Rayleigh/LIF Measurements in a Turbulent CH₄/H₂/N₂ Jet Diffusion Flame: Experimental Techniques and Turbulence-Chemistry Interaction*. Combust. Flame, 123(2000):326-343, 2000.
- [21] W. G. BESSLER, C. SCHULZ, T. LEE, D.-I. SHIN, M. HOFMANN, J. B. JEFFRIES, J. WOLFRUM and R. K. HANSON – *Quantitative NO-LIF Imaging in High-Pressure Flames*. Appl. Phys. B, 75:97-102, 2002.
- [22] V. M. VAN ESSEN, A.V. SEPMAN, A.V. MOKHOV and H.B. LEVINSKY – *The Effects of Burner Stabilization on Fenimore NO Formation in Low-Pressure, Fuel-Rich Premixed CH₄/O₂/N₂ Flames*. Proc. Combust. Inst., 31(2007):329-337, 2007.
- [23] H. BOCKHORN – *Soot Formation in Combustion, Mechanisms and Models*. Springer Series in Chemical Physics 59, Springer-Verlag.
- [24] R. J. SANTORO, H. G. SEMERJIAN and R. A. DOBBINS – *Soot Particle Measurements in Diffusion Flames*. Combust. Flame, 51(1983):203-218, 1983.
- [25] U. VANDSBURGER, I. KENNEDY and I. GLASSMAN – *Sooting Counterflow Diffusion Flames with Varying Oxygen Index*. Comb. Sci. Tech., 39, (1984):263-285, 1984.
- [26] B. QUAY, T.-W. LEE, T. NI and R. J. SANTORO – *Spatially Resolved Measurements of Soot Volume Fraction Using Laser-Induced Incandescence*. Combust. Flame, 97(1994):384-392, 1994.
- [27] C. S. MCENALLY and L. D. PFEFFERLE – *Experimental Study of Nonfuel Hydrocarbons and Soot in Coflowing Partially Premixed Ethylene/Air Flames*. Combust. Flame, 121(2000):575-592, 2000.
- [28] C. P. ARANA, M. PONTONI, S. SEN and I. K. PURI – *Field Measurements of Soot Volume Fractions in Laminar Partially Premixed Coflow Ethylene/Air Flames*. Combust. Flame, 138(2004):362-372, 2004.
- [29] L. L. MCCRAIN and W. L. ROBERTS – *Measurements of the Soot Volume Field in Laminar Diffusion Flames at Elevated Pressures*. Combust. Flame, 140(2005):60-69, 2005.
- [30] K. A. THOMSON, Ö. L. GÜLDER, E. J. WECKMAN, R. A. FRASER, G. SMALLWOOD and D. R. SNELLING – *Soot Concentration and Temperature Measurements in Co-Annular, Nonpremixed CH₄/Air Laminar Flames at Pressures up to 4 MPa*. Combust. Flame, 140(2005):222-232, 2005.
- [31] P. DESGROUX, X. MERCIER, B. LEFORT, R. LEMAIRE, E. THERSSEN and J.F. PAUWELS – *Soot Volume Fraction Measurement in Low-Pressure Methane Flames by Combining Laser-Induced Incandescence and Cavity Ring-Down Spectroscopy: Effect of Pressure on Soot Formation*. Combust. Flame, 155(2008):289-301, 2008.
- [32] H. I. JOO and Ö. L. GÜLDER – *Soot Formation and Temperature Field Structure in Co-Flow Laminar Methane-Air Diffusion Flames at Pressures from 10 to 60 Atm*. Combust. Flame, 32(2009):769-775, 2009.

- [33] K. M. LEUNG, R. P. LINDSTEDT and W. P. JONES – *A Simplified Reaction Mechanism for Soot Formation in Nonpremixed Flames*. Combust. Flame, 87(1991):289-305, 1991.
- [34] T. BLACHA, M. DI DOMENICO, P. GERLINGER and M. AIGNER – *Soot Predictions in Premixed And Non-Premixed Laminar Flames Using a Sectional Approach For PAHs And Soot*. Combust. Flame, 159(2012):181-193, 2012.
- [35] C. R. SHADDIX and K. C. SMYTH – *Laser-Induced Incandescence Measurements of Soot Production in Steady and Flickering Methane, Propane, and Ethylene Diffusion Flames*. Combust. Flame, 107(1996):418-452, 1996.
- [36] N.H. QAMAR, Z. T. ALWAHABI, Q. N. CHAN, G. J. NATHAN, D. ROEKAERTS and K. D. KING – *Soot Volume Fraction in a Piloted Turbulent Jet Non-Premixed Flame of Natural Gas*. Combust. Flame, 156(2009):1339-1347, 2009.
- [37] R. LEMAIRE, A. FACCINETTO, E. THERSSEN, M. ZISKIND, C. FOCSA and P. DESGROUX – *Experimental Comparison of Soot Formation in Turbulent Flames of Diesel and Surrogate Diesel Fuels*. Combust. Flame, 32(2009):737-744, 2009.
- [38] T. L. HENRIKSEN, G. J. NATHAN, Z. T. ALWAHABI, N. QAMAR, T. A. RING and E. G. EDDINGS – *Planar Measurements of Soot Volume Fraction and OH in a JP-8 Pool Fire*. Combust. Flame, 156(2009):1480-1492, 2009.
- [39] M. KÖHLER, K.P. GEIGLE, T. BLACHA, P. GERLINGER and W. MEIER – *Experimental Characterization and Numerical Simulation of a Sooting Lifted Turbulent Jet Diffusion Flame*. Combust. Flame, 159(2012):2620-2635, 2012.
- [40] M. E. MUELLER, Q. N. CHAN, N. H. QAMAR, B. B. DALLY, H. PITSCH, Z. T. ALWAHABI and G. J. NATHAN – *Experimental and Computational Study of Soot Evolution in a Turbulent Nonpremixed Bluff Body Ethylene Flame*. Combust. Flame, 160(2013):1298-1309, 2013.
- [41] K.P. GEIGLE, R. HADEF and W. MEIER – *Soot Formation and Flame Characterization of an Aero-Engine Model Combustor Burning Ethylene at Elevated Pressure*. J. Eng. Gas Turbines Power 136(2014), 021505, 2014.
- [42] K.P. GEIGLE, M. KÖHLER, W. O'LOUGHLIN and W. MEIER – *Investigation of Soot Formation In Pressurized Swirl Flames by Laser Measurements of Temperature, Flame Structures and Soot Concentrations*. Proc. Combust. Inst., 35(2015):3373-3380, 2015.
- [43] K.P. GEIGLE, W. O'LOUGHLIN, R. HADEF and W. MEIER – *Visualization of Soot Inception in Turbulent Pressurized Flames by Simultaneous Measurement of Laser-Induced Fluorescence of Polycyclic Aromatic Hydrocarbons and Laser-Induced Incandescence, and Correlation to OH Distributions*. Appl. Phys. B 119(2015):717-730, 2015.
- [44] R. SAID, A. GARO and R. BORGHI – *Soot Formation Modeling for Turbulent Flames*. Combust. Flame, 108(1997):71-86, 1997.
- [45] H. PITSCH, E. RIESMEIER and N. PETERS – *Unsteady Flamelet Modeling of Soot Formation in Turbulent Diffusion Flames*. Comb. Sci. and Tech., 158, Issue1(2000):389-406, 2000.
- [46] B. ZAMUNER and F. DUPOIRIEUX – *Numerical Simulation of Soot Formation in a Turbulent Flame with a Monte-Carlo PDF Approach and Detailed Chemistry*. Comb. Sci. and Tech., 158, Issue 1(2000):407-438, 2000.
- [47] C. S. YOO and H. G. IM – *Transient Soot Dynamics in Turbulent Nonpremixed Ethylene–Air Counterflow Flames*. Proc. Combust. Inst., 31(2007):701-708, 2007.
- [48] D. O. LIGNELL, J. H. CHEN and P. J. SMITH – *Three-Dimensional Direct Numerical Simulation of Soot Formation and Transport in a Temporally Evolving Nonpremixed Ethylene Jet Flame*. Combust. Flame, 155(2008):316-333, 2008.
- [49] P. NARAYANAN and A. TROUVÉ – *Radiation-Driven Flame Weakening Effects in Sooting Turbulent Diffusion Flames*. Combust. Flame, 32(2009):1481-1489, 2009.
- [50] F. BISETTI, G. BLANQUART, M. E. MUELLER and H. PITSCH – *On the Formation and Early Evolution of Soot in Turbulent Nonpremixed Flames*. Combust. Flame, 159(2012):317-335, 2012.
- [51] M. E. MUELLER and H. PITSCH – *LES Model for Sooting Turbulent Nonpremixed Flames*. Combust. Flame, 159(2012):2166-2180, 2012.
- [52] A. ATTILI, F. BISETTI, M. E. MUELLER and H. PITSCH – *Damköhler Number Effects on Soot Formation and Growth in Turbulent Nonpremixed Flames*. Combust. Flame, 35(2015):1215-1223, 2015.
- [53] F. DUPOIRIEUX, N. BERTIER, A. BOUCHER and P. GILBANK – *A Cost-Effective Backward Lagrangian Method for Simulation of Pollutant Formation in Gas Turbine Combustors by Post-Processing of Complex 3D Calculations*. Int. J. Sustainable Aviation, 1,(2014):160-180, 2014.
- [54] H. BARTHIS, N. PETERS, N. BREHM, A. MACK, M. PFITZNER and V. SMILJANOVSKI – *Simulation of Pollutant Formation in a Gas-Turbine Combustor Using Unsteady Flamelets*. Proc. Combust. Inst., 27(1998):1841-1847, 1998.
- [55] M. E. MUELLER and H. PITSCH – *Large Eddy Simulation of Soot Evolution in an Aircraft Combustor*. Physics of Fluids, 25, 110812, 2013.
- [56] A. REFLOCH, B. COURBET, A. MURRONE, P. VILLEDIEU, C. LAURENT, P. GILBANK, J. TROYES, L. TESSÉ, G. CHAINERAY, J.B. DARGAUD, E. QUÉMERAIS and F. VUILLOT – *CEDRE Software*. Aerospace Lab, Issue 2, 2011.
- [57] L. SELLE, G. LARTIGUE, T. POINSOT, R. KOCH, K.-U. SCHILDMACHER, W. KREBS, B. PRADE, P. KAUFMANN and D. VEYNANTE – *Compressible Large Eddy Simulation of Turbulent Combustion in Complex Geometry on Unstructured Meshes*. Combust. Flame, 137(2004):489-505, 2004.
- [58] O. COLIN, F. DUCROS, D. VEYNANTE and T. POINSOT – *A Thickened Flame Model for Large Eddy Simulations of Turbulent Premixed Combustion*. Physics of Fluids, Vol. 12, No. 7(2000):1843-1863, 2000.
- [59] U. MAAS and S. B. POPE – *Simplifying Chemical Kinetics: Intrinsic Low-Dimensional Manifolds in Composition Space*. Combust. Flame, 88(1992):239-264, 1992.
- [60] O. GICQUEL, N. DARABIHA and D. THÉVENIN – *Laminar Premixed Hydrogen/Air Counterflow Flame Simulations Using Flame Prolongation of ILDM with Differential Diffusion*. Proc. Combust. Inst., 28(2000):1901-1908, 2000.
- [61] J. A. VAN OIJEN, F. A. LAMMERS and L. P. H. DE GOEY – *Modeling of Complex Premixed Burner Systems by Using Flamelet-Generated Manifolds*. Combust. Flame, 127(2001):2124-2134, 2001.
- [62] B. FIORINA, O. GICQUEL, L. VERVISCH, S. CARPENTIER and N. DARABIHA – *Premixed Turbulent Combustion Modeling Using Tabulated Detailed Chemistry and PDF*. Combust. Flame, 30(2005):867-874, 2005.
- [63] G. KUENNE, A. KETELHEUN and J. JANICKA – *LES Modeling of Premixed Combustion Using a Thickened Flame Approach Coupled with FGM Tabulated Chemistry*. Combust. Flame, 158(2011):1750-1767, 2011.
- [64] A. W. VREMAN, B. A. ALBRECHT, J. A. VAN OIJEN, L. P. H. DE GOEY and R. J. M. BASTIAANS – *Premixed and Nonpremixed Generated Manifolds in Large-Eddy Simulation of Sandia Flame D and F*. Combust. Flame, 153(2008):394-416, 2008.
- [65] A. BOUCHER, N. BERTIER and F. DUPOIRIEUX – *A Method to Extend Flamelet Manifolds for Prediction of NOx And Long Time Scale Species with Tabulated Chemistry*. Int. J. Sustainable Aviation, vol. 1, n° 2(2014):181-202, 2014.

- [66] B. F. MAGNUSSEN and B. H. HJERTAGER – *On Mathematical Modeling on Turbulent Combustion with Special Emphasis on Soot Formation and Combustion*. Proc. Combust. Inst., 16(1977):719-729, 1977.
- [67] G. LECOQ, D. POITOU, I. HERNANDEZ, F. DUCHAINE, E. RIBER and B. CUENOT – *A Methodology for Soot Prediction Including Thermal Radiation in Complex Industrial Burners*. Flow Turbulence Combust., 92(2014):947-970, 2014.
- [68] B. CUENOT, R. VICQUELIN, E. RIBER, V. MOUREAU, G. LARTIGUE, A. FIGUER, Y. MERY, J. LAMOUREUX, S. RICHARD, L. GICQUEL, T. SCHMITT and S. CANDEL – *Advanced Simulation of Combustion in Aeronautical Burners*. Aerospace Lab, Issue 11, 2016.
- [69] N. A. SLAVINSKAYA and O. J. HAIDN – *Reduced Chemical Model for High Pressure Methane Combustion with PAH Formation*. Proc. 46th AIAA Aerospace Sciences Meeting, n° AIAA 2008-1012, 2008.
- [70] M. DI DOMENICO, P. GERLINGER and M. AIGNER – *Development and Validation of a New Soot Formation Model for Gas Turbine Combustor Simulations*. Combust. Flame 157(2010): 246–258, 2010.
- [71] K.P. GEIGLE, R. HADEF, M. STÖHR and W. MEIER – *Flow Field Characterization of Pressurized Sooting Swirl Flames and Correlation to Soot Distributions*. Proc. Combust. Inst., 2016.
- [72] S. TROTTIER, H. GUO, G. J. SMALLWOOD and M. R. JOHNSON – *Measurement and Modeling of the Sooting Propensity of Binary Fuel Mixtures*. Proc. Combust. Inst. 31(2007):611-619, 2007.
- [73] M. S. TSURIKOV, K.-P. GEIGLE, V. KRÜGER, Y. SCHNEIDER-KÜHNLE, W. STRICKER, R. LÜCKERATH, R. HADEF and M. AIGNER – *Laser-Based Investigation of Soot Formation in Laminar Premixed Flames at Atmospheric and Elevated Pressures*. Combust. Sci. Technol., 177(2005):1835-1862, 2005.
- [74] A. COCHET, C. GUIN, A. VINCENT, O. DESSORNES, A. BRESSON, M. ORAIN and C. BROSSARD – *ONERA Test Facilities for Combustion in Aero Gas Turbine Engines and Associated Optical Diagnostics*. Aerospace Lab, issue 11, 2016.
- [75] FP6-TLC, 2005-2010, http://ec.europa.eu/research/transport/projects/items/tlc_en.htm.
- [76] M. ORAIN, F. GRISCH, E. JOURDANNEAU, B. ROSSOW, C. GUIN and B. TRÉTOU – *Simultaneous Measurements of Equivalence Ratio and Flame Structure in Multipoint Injectors Using PLIF*. C. R. Mecanique, 337(2009):373-384, 2009.
- [77] K. P. GEIGLE, J. ZERBS and C. GUIN – *Laser-Induced Incandescence for Soot Measurements in Technical Flames at Increased Pressure at the ONERA M1 Test Rig*. Proc. Deutscher Luft- und Raumfahrtkongress 2010, Paper 1235, 31.08.-02.09.2010, 2010.
- [78] A. J. CHORIN – *Numerical Solution of the Navier-Stokes Equations*. Mathematics of Computation, 22,104(1968):745–762, 1968.
- [79] F. R. MENTER – *Two-Equation Eddy-Viscosity Turbulence Models for Engineering Applications*. AIAA Journal, 32(1994):1598–1605, 1994.
- [80] P. GERLINGER – *Investigation of an Assumed PDF Approach for Finite-Rate Chemistry*. Combust. Sci. Technol., 175(2003):841–872, 2003.
- [81] C. EBERLE, P. GERLINGER, K. P. GEIGLE and M. AIGNER – *Numerical Investigation of Transient Soot Evolution Processes in an Aero-Engine Model Combustor*. Combust. Sci. Technol., 187(2015):1841–1866, 2015.
- [82] J. LUCHE, M. REUILLON, J.-C. BOETTNER and M. CATHONNET – *Reduction of Large Detailed Kinetic Mechanisms: Application to Kerosene/Air Combustion*. Comb. Sci. and Tech., 176 (11)(2004):1935-1963, 2004.
- [83] L.-H. DOREY – *Modélisation des phénomènes couplés combustion-formation des suies-transferts radiatifs dans les chambres de combustion de turbine à gaz*. Thèse de l'Ecole Centrale Paris, Energétique, 2012.
- [84] J. VAN OIJEN and L. DE GOEY – *Predicting NO Formation with Flamelet Generated Manifolds*. Proc. European Combustion Meeting, 2009.
- [85] A. BOUCHER – *Modélisation de la formation des polluants au sein des foyers aéronautiques par une méthode de chimie tabulée*. Thèse de l'Ecole Centrale Paris, Energétique, 2015.

Acknowledgement

This work has been funded by ONERA, the ANR (French National Research Agency) and the European Commission within the project Fuel Injector Research for Sustainable Transport (FIRST) under contract No. 265848. The authors gratefully acknowledge the computing time granted on the supercomputer JUROPA at Jülich Supercomputing Centre (JSC).

Acronyms

CARS (Coherent Anti-stokes Raman Spectroscopy)	LES (Large Eddy Simulation)	PAH (Polycyclic Aromatic Hydrocarbon)
FAR (Fuel Air Ratio)	LII (Laser Induced Incandescence)	URANS (Unsteady Reynolds-Averaged Navier-Stokes resolution)
GT combustor (Gas Turbine combustor)	OPR (Operating Pressure Ratio)	

Nomenclature

c	progress variable	t	time, s	x_i	spatial coordinate, m
D_k	diffusion coefficient, m ² /s	T	temperature, K	X	mass fraction
M_k	molar mass, kg	u_i	velocity component, m/s	Z	mixture fraction

Greek Letters

ρ	mixture density, kg/m ³
ρ_{soot}	soot density, kg/m ³
M_k	chemical reaction rate, kg m ⁻³ s ⁻¹
$\dot{\omega}_k$	temperature, K

Subscripts

i	$i=1,2,3$, spatial direction
k	chemical species

Superscripts

TAB	value picked from the chemical table
-------	--------------------------------------



Francis Dupoirieux is deputy head of the Energetics department of ONERA, in charge of the scientific management of the activity. He created 3D CFD tools for the numerical simulation of turbulent reactive flows that have been widely used by research laboratories and industrial partners of ONERA. He also developed physical models of pollutant formation in flames. He is now involved in the development of the CEDRE code, dedicated to multiphysics problems in reactive flows. This task includes the definition of experiments for validating the models implemented in CEDRE and the global validation of this code. He is teaching thermodynamics and thermal transfer at the École Centrale Paris.



Nicolas Bertier, graduated from ENS Cachan and PhD from Paris VI University, is senior researcher in the Energetics department of ONERA. He is in charge of the numerical simulation of reactive flows in aeronautic combustors. He has developed and validated the numerical methods and combustion models required to carry out LES with the CEDRE code of ONERA. He is the leader of the CEDRE project. He is also teaching “energetics of aeronautic combustors” at Paris VI University and ISAE Toulouse.



Christian Guin graduated Engineer in 1980 from CNAM (Conservatoire National des Arts et Métiers). He joined ONERA in 1974 as technician and, since 1980, has been working as research engineer in the Energetic Department. He was involved in experimental combustion studies for ducted rocket and ramjet, and then, since 1995, on new combustor concepts for turbojet. He has developed the M1 high pressure test facility, devoted to the turbojet combustors studies at ONERA, and is in charge of the experiments carried out on this facility.



Luc-Henry Dorey is a research engineer at ONERA, working in the Fundamental and Applied Energetics Department (DEFA). He graduated from ISAE-ENSMA (Poitiers) in 2008 and received his PhD degree in energetics from Ecole Centrale Paris in 2012. His research field is mainly focused on combustion, acoustics, soot formation and two-phase flow modeling for CFD simulation of liquid-propellant rocket engines and gas turbines.



Klaus Peter Geigle received his PhD in Physical Chemistry, specifically on laser-based characterization of PAH, at the University of Cologne. Since 1999 he is focussing on experimental characterization of sooting atmospheric and pressurized flames at DLR as member of the department of combustion diagnostics. Main tool of those flame studies is laser-induced incandescence which he develops and applies in laboratory applications as well as at test rigs at other sites. The generated detailed and accurate data sets frequently serve for validation of numerical combustion models.



Christian Eberle graduated at the University of Stuttgart and since 2011 he is PhD student at the DLR institute of combustion technology. His PhD supervisor is Peter Gerlinger. The focus of Christian’s research is the development and validation of predictive soot models for CFD applications.



Peter Gerlinger received his PhD 1994 in aeronautical engineering from the University of Stuttgart. He obtained in 2004 the habilitation in combustion technology and, since 2015, is apl. Professor at the University of Stuttgart. Main research topics are high order numerical simulation, turbulence chemistry interaction, convergence acceleration, and soot modeling.